

**Department of Physics and Astronomy
Heidelberg University**

Bachelor Thesis in Physics
submitted by

Nicola Wilson

born in Walsrode (Germany)

2022

Phenomenological study of J/Ψ emission in p-Pb collisions at the LHC

This Bachelor Thesis has been carried out by Nicola Wilson at the
Physikalisches Institut in Heidelberg
under the supervision of
Prof. Dr. Klaus Reygers

Abstract

The emission pattern of J/Ψ mesons in p-Pb collisions as a function of the center-of-mass system with changing centralities was studied. A Glauber Monte Carlo calculation and p-p data for different $\sqrt{s_{NN}}$ are the basis for the simulation. Two scenarios were studied. The first one assumes energy loss of the incoming proton in each binary collision with a Pb nucleon. The energy loss is hereby described using an exponential function dependend on the number of collisions adjusted to match the measured charged-particle p-Pb pseudorapidity distribution. The second one regards the participating part of the Pb nucleus as a massive target which is hit by the proton. The Monte Carlo simulation is compared to ALICE data in terms of the mean transverse momentum and the J/Ψ yield as a function of the number of produced charged particles.

Zusammenfassung

Das Emissionsverhalten von J/Ψ Mesonen in Proton-Blei Kollisionen in Abhängigkeit des Massenschwerpunktssystems mit verschiedenen Zentralitäten wird untersucht. Eine Glauber Monte Carlo Simulation und Daten aus p-p Kollisionen für verschiedene $\sqrt{s_{NN}}$ sind die Basis dieser Simulation. Zwei Szenarien wurden untersucht. Im ersten wird angenommen, dass das eingehende Proton in jeder Kollision mit einem Bleinukleon seine Energie verringert. Die Energie wird hierbei durch eine Exponentialfunktion beschrieben, welche von der Anzahl der Kollisionen abhängt und angepasst wurde, sodass sie zu der p-Pb Pseudorapiditätsverteilung passt. In dem zweiten Modell wird der an der Kollision teilnehmende Teil des Bleikerns als massives Target betrachtet, welches von dem Proton getroffen wird. Die p_T Verteilung und die Anzahl der J/Ψ Mesonen in Abhängigkeit der Anzahl der geladenen Teilchen resultierend aus der Simulation werden mit ALICE-Daten verglichen.

Contents

1	Introduction	1
1.1	The Standard model	1
1.2	The J/Ψ Meson	3
1.3	Kinematics and collisions	4
1.4	ALICE publication	7
1.5	Structure	9
2	Glauber Monte Carlo simulation	10
2.1	Simulation of p-Pb collisions	10
2.2	Collision profiles	11
2.3	Results from the Glauber simulation	12
3	Multiple collision model	17
3.1	First steps	17
3.2	Generation of charged particles	17
3.3	η distribution	23
3.4	Applying the boost	29
4	Results	30
4.1	$p_T - \eta$ distributions	30
4.2	Mean transverse momentum	31
4.3	J/Ψ yield	32
4.4	Massive target model	33
	4.4.1 Results	34
4.5	Comparison	35
5	Conclusion and Outlook	37
6	Appendix	39
6.1	Kinematics	39

1 Introduction

1.1 The Standard model

All the visible matter surrounding us is made out of atoms. Atoms have long been thought to be the smallest unit of matter, therefore the name "atom" which comes from the greek "átomos", meaning indivisible. But experiments have shown that this assumption was not true and there are even smaller units [1].

In table 1 a brief historic overview on the development of particle physics can be found.

1896	First forms of radioactivity observed by Antoine Becquerel
1898	Discovery of Polonium and Radium by Marie and Pierre Curie
1902-1909	Existence of three types of radioactive decay was shown by Ernest Rutherford and Frederick Soddy
1911	Scattering experiment with α -particles on gold foil by E. Rutherford resulting in an atomic theory
1911	Discovery of isotopes by Joseph Thomson
1932	Discovery of the neutron by James Chadwick
1939	Discovery of nuclear fission by Otto Hahn and Fritz Straßmann
1969	Establishment of quark hypothesis by Gell-Mann and Zweig

Table 1: Historic overview of nuclear and particle research [1].

The main knowledge about particles is summarized in the standard model of particle physics that describes elementary particles and the three fundamental forces that they interact with [2]. Elementary particles can be classified into two groups which are the fermions and the bosons. Fermions have a half integer spin and are again subcategorized into leptons and quarks. The so called first generation consists of the electron e^- , electron neutrino ν_e , the up quark u and down quark d . There are two more generations which are copies of the first generation but with higher masses [2]. An overview of all the fermions can be found in table 2.

	Leptons			Quarks		
	Particle	Charge	Mass (GeV)	Particle	Charge	Mass (GeV)
1. Generation	electron (e^-)	-1	0.0005	down (d)	-1/3	0.003
	neutrino (ν_e)	0	$< 10^{-9}$	up (u)	+2/3	0.005
2. Generation	muon (μ^-)	-1	0.106	strange (s)	-1/3	0.1
	neutrino (ν_μ)	0	$< 10^{-9}$	charm (c)	+2/3	1.3
3. Generation	tau (τ^-)	-1	1.78	bottom (b)	-1/3	4.5
	neutrino (ν_τ)	0	$< 10^{-9}$	top (t)	+2/3	174

Table 2: Overview of fermions [2].

For every fermion discussed in the previous section, there also exists an anti-particle with the same mass but opposite charge. They are indicated by a bar, for example \bar{d} for the anti-down quark, or by the charge, for example e^+ for the positron as antiparticle of the electron e^- .

The three fundamental forces are the electromagnetic, strong and weak interaction and are each described by a quantum field theory (QFT). They are mediated by gauge bosons that have an integer spin [2].

The weak interaction is divided into the weak charged-current interaction carried out by the charged W^+ , W^- bosons with mass $m = 80.4$ GeV and the weak neutral-current interaction mediated by the neutral Z boson with $m = 91.2$ GeV. The $W^{+/-}$ bosons have the charges $+/- e$ and due to charge conservation, they can only couple fermions with a charge difference of e . For leptons, this

means that charged leptons will be coupled with their corresponding neutrino while quarks can be coupled in multiple ways as long as the electrical charge is conserved. The weak charged-current interaction is responsible for particle decays, since it is the only interaction allowing a change in the particles flavour.

In case of the electromagnetic interaction, the corresponding gauge boson is the massless photon γ with spin 1. The matching QFT is quantum electrodynamics (QED). Every charged particle undergoes the electromagnetic interaction, meaning every fermion apart from the (anti-) neutrinos. The strong interaction is transmitted by the massless gluon g and is described by quantum chromodynamics (QCD). The charge of this interaction is the colour charge which can be green, red or blue. Only quarks and gluons carry colour charge which is the reason why only they participate in the strong interaction. The gluon's colour charge consists of a colour and an anti colour. Unlike photons that carry no charge, the gluons can self interact because of their colour charge [2].

When separating two quarks that interact by exchanging gluons, the exchanging gluons undergo attractive interactions with each other as indicated in figure 1a. The field lines are then not spread like in QED (figure 1b) but confined into a tube (1c). The energy stored in this gluon field is proportional to the distance which leads to vast energies at macroscopic distances [2].

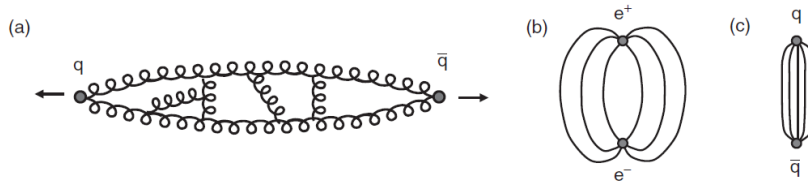


Figure 1: Representation of gluon self interaction (a), field lines in electromagnetic interaction (b) and in QCD (c) [2].

As a consequence, quarks are confined to colourless bound states which are called hadrons. The hadrons consisting of two quarks are called mesons while the hadrons made of three quarks are called baryons. The most commonly known baryons are the neutron (udd) and the proton (uud) which is the only stable hadron. There also exist antibaryons, made of three antiquarks. Hadrons are always colourless so that there is no colour fields between them, meaning they consist either of all three colours or a colour and its anti colour [2]. In contrast in the so called Quark Gluon Plasma (QGP), quarks and gluons are not confined and can move quasi freely. This state was supposed to occur right after the Big Bang followed by forming hadronic matter at lower temperature and density. The QGP can be reproduced in laboratories with heavy ion collisions where high energy densities and temperatures are reached [3].

The Higgs boson is the most recently discovered element of the standard model. Its mass is $m \approx 125$ GeV and unlike all other discovered particles, it is a scalar particle with spin 0. The Higgs boson is essential for other particles to acquire mass [2].

At this point, the standard model of particle physics seems to be the best description regarding subatomic structures, but still it is not complete. It does not include the fourth fundamental force, gravity. Some physicists assume that there is a gauge boson named graviton G which mediates gravitational force. It is supposed to be a massless spin-2 particle but could never be confirmed experimentally [4][2].

The standard model also does not explain dark matter. It is not visible since it does not interact with the electromagnetic force, therefore it is hard to measure. Its existence was expected due to gravitational effects that it has on visible matter [5].

1.2 The J/Ψ Meson

In 1974, the group of Burton Richter, Stanford University, made an unexpected discovery at the Stanford Linear Accelerator Center (SLAC) at the electron-positron storage ring SPEAR. In the cross section of $e^+e^- \rightarrow \text{hadrons}$, e^+e^- and probably $\mu^+\mu^-$ a sharp peak was found. This structure with energy $E = 3.105 \pm 0.003$ GeV and upper limit of the full width at half maximum $\Gamma \leq 1.3$ MeV was proposed to be named Ψ [6].

In the same year, Samuel C. C. Ting and his group were looking for particles decaying into e^+e^- and $\mu^+\mu^-$ pairs at the Brookhaven National Laboratory's alternating-gradient synchrotron. There was found a clear peak in the mass spectrum at around $m = 3.1$ GeV, which was assumed to be a particle that they called J decaying into an e^+e^- pair. Some further tests were made to reassure that it is a real particle, for example reducing the beam intensity, making cuts in the data or decreasing the magnet currents. The group has also seen the possibility that this was a charmed particle whose existence was theoretically predicted [7].

Due to the almost simultaneous discovery of this particle, it is now called J/Ψ and in 1976, both B. Richter and S. Ting were awarded the Nobel Prize for physics [8].

Just as S. Ting assumed, the discovery of the J/Ψ meson was the proof of the existence of the charm quark c . The J/Ψ is a quarkonium, more precisely charmonium, meaning it consists of a charm quark c and an anti charm quark \bar{c} . Its mass is $m = 3096.900 \pm 0.006$ MeV and its full width is $\Gamma = 92.9 \pm 2.8$ keV. Their main decay modes are hadrons with (87.7 ± 0.5) %, an e^+e^- pair with (5.971 ± 0.032) % and a $\mu^+\mu^-$ pair with (5.961 ± 0.033) % [9].

Studying the J/Ψ meson is relevant because it can be seen as a probe of the QGP forming in a nuclear collision. If in a hadron-hadron collision a $c\bar{c}$ pair is produced, this would lead to J/Ψ production. If in the same collision a QGP is formed, the J/Ψ formation would be initially suppressed because of the Debye screening of colour charge. At sufficiently high temperatures, the screening radius $r_D(T)$ can be smaller than the binding radius $r_{J/\Psi}(T)$ of the J/Ψ meson which then results in prohibiting J/Ψ production [10].

In heavy ion collisions where a QGP forms, the number of emerging $c\bar{c}$ pairs depends on the center-of-mass energy. With increasing energy, the charm production cross section also increases which is indicated in the first column of figure 2 [11]. In the following QGP formation the charm quarks are deconfined. At lower energies the few (anti) charm quarks tend to hadronize into D mesons due to the lack of $c\bar{c}$ partons. At higher energies, the (anti) charm quark density is higher, therefore in addition to the D mesons J/Ψ mesons form. This kind of behaviour was predicted with a statistical hadronization model (SHM) and can be measured using the nuclear modification factor [11].

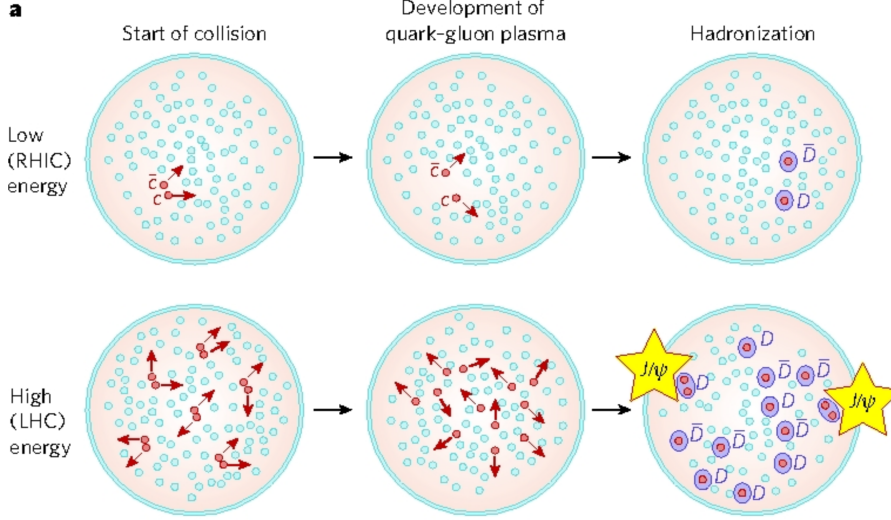


Figure 2: Quarkonia production in collisions at low and high energies [12].

The nuclear modification factor $R_{AA}^{J/\Psi}$ is shown as a function of the charged particle multiplicity density per pseudorapidity in figure 3. It is defined as the ratio between the J/Ψ yield in nucleus-nucleus (A-A) collisions and the superposition of the J/Ψ yield in nucleon-nucleon (p-p) collisions [13].

$$R_{AA}^{J/\Psi} = \frac{dN_{J/\Psi}^{AA}/dy}{N_{coll} \cdot dN_{J/\Psi}^{pp}/dy} \quad (1)$$

Here it is also visible that at low energies (RHIC) there is a J/Ψ suppression, the factor $R_{AA}^{J/\Psi}$ is decreasing with increasing charged particle multiplicity density. In contrast at higher energies (LHC) there is an enhancement relative to lower energies which is indicated by a higher $R_{AA}^{J/\Psi}$.

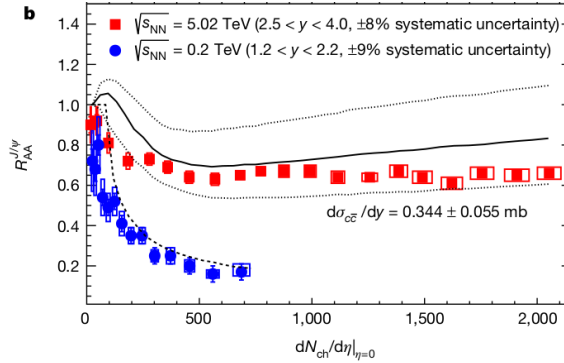


Figure 3: Relative J/Ψ yield $R_{AA}^{J/\Psi}$ dependent on the charged particle multiplicity density per pseudorapidity. Red markers: Pb-Pb collision measured at ALICE at $\sqrt{s_{NN}} = 5.02$ TeV. Blue markers: Au-Au collisions measured at RHIC at $\sqrt{s_{NN}} = 0.2$ TeV [14].

1.3 Kinematics and collisions

If a system moves at high velocities v near the velocity of light $c = 299792458 \frac{m}{s}$, the effects of special relativity have to be considered. In this case, two measures are often used [2]:

$$\beta = \frac{v}{c} \quad (2)$$

$$\gamma = \frac{1}{\sqrt{1 - \beta^2}} \quad (3)$$

In relativistic kinematics, it is helpful to describe systems not only by a three component vector, but by a four-vector. Most commonly used is the contravariant space-time four-vector x^μ [2]:

$$x^\mu = (x^0, x^1, x^2, x^3) = (t, \vec{x}) = (t, x, y, z) \quad (4)$$

There also is the covariant space-time four-vector which is indicated by the lower index and which differs by the signs from the contravariant version [2]:

$$x_\mu = (t, -x, -y, -z) \quad (5)$$

The momentum-energy four-vectors are also contravariant and can be written as

$$p^\mu = (p^0, p^1, p^2, p^3) = (E, \vec{p}) = (E, p_x, p_y, p_z) \quad (6)$$

where it was assumed that $c = 1$. Due to the conservation of energy and momentum, the four-momentum is also conserved.

If one system S', described by the four-vector $x^{\mu'} = (x^{0'}, x^{1'}, x^{2'}, x^{3'})$ moves relative to another system S, described by $x^\mu = (x^0, x^1, x^2, x^3)$, with velocity β , a Lorentz transformation is needed to transform the coordinates from S' to S. In case S' is only moving in x^3 -direction, the transformation is given by [2]

$$\begin{aligned} x^{0'} &= \gamma(x^0 - \beta x^3) \\ x^{1'} &= x^1 \\ x^{2'} &= x^2 \\ x^{3'} &= \gamma(x^3 - \beta x^0) \end{aligned} \quad (7)$$

Contravariant vectors are related by this Lorentz transformation when measured in two inertial frames. If two four-vectors a and b are contravariant, then their scalar product is Lorentz-invariant and can be written as [2]:

$$a \cdot b = a^\mu b_\mu = a_\mu b^\mu = a^0 b^0 - \vec{a} \cdot \vec{b} \quad (8)$$

Which leads the energy momentum four-vector to be

$$p \cdot p = E^2 - \vec{p}^2 \quad (9)$$

If a single particle is at rest, its four-momentum is $p^\mu = (m, 0, 0, 0)$ which results in $p^\mu p_\mu$ being equal to the squared mass m^2 . Because of the Lorentz invariance of this quantity and equation 9, the relation between energy, momentum and mass can be written as

$$E^2 - \vec{p}^2 = m^2 \quad (10)$$

where the mass is called invariant mass because it remains equal in every frame. The mass of a decaying particle, e.g. $J/\Psi \rightarrow e^+e^-$, can therefore be calculated from the energy and momentum of the decay products [15].

There are three variables, called the Mandelstam variables s, t and u, that characterize collisions where the two incoming particles have the Four-vector p_1 and p_2 and the outgoing particles

p_3 and p_4 [2]:

$$s = (p_1 + p_2)^2 = (p_3 + p_4)^2 \quad (11)$$

$$t = (p_1 - p_3)^2 = (p_2 - p_4)^2 \quad (12)$$

$$u = (p_1 - p_4)^2 = (p_2 + p_3)^2 \quad (13)$$

The quantity \sqrt{s} is the total center-of-mass energy [2]. In the center-of-mass frame, where $\vec{p}_1 = -\vec{p}_2$ holds, s is given by

$$s = (p_1 + p_2)^2 = (E_1 + E_2)^2 \quad (14)$$

A measure for the probability of an interaction happening is the cross section σ which has the dimension of area. If a beam of particles a has the flux ϕ_a , meaning the number of particles that traverse a unit area in a unit time, then the interaction rate r is given as [2]:

$$r = \sigma \phi_a \quad (15)$$

The cross section is defined as the number of interactions per unit time per target particle divided by the incident flux. The commonly used unit is barn b with $1 b = 10^{-28} \text{ m}^2 = 100 \text{ fm}^2$ [2]. If the distribution of a kinetic variable, for example the angular distribution, is relevant the differential cross section $\frac{d\sigma}{d\Omega}$ can be taken into account. It is defined almost as before but with the difference, that the number of particles scattered into $d\Omega$ instead of the total number of interactions is taken. In this analysis, the geometric cross section was used. It is defined with the radius of the target r_t and the radius of the projectile r_p in the following manner [2]:

$$\sigma = \pi(r_t + r_p)^2 \quad (16)$$

Two important measures regarding particle or heavy ion collisions are the rapidity y and the pseudorapidity η .

The former characterizes the longitudinal velocity:

$$\begin{aligned} y &= \tanh^{-1}(\beta_L) \\ &= \frac{1}{2} \ln \left(\frac{E + p_L}{E - p_L} \right) \end{aligned} \quad (17)$$

The rapidity y is not Lorentz invariant, meaning it does not transform as in equation 7, but still has a simpler Lorentz transformation than the velocity u . This is a reason to use rapidity y instead of velocity u . When a system S' moves with β , the rapidity in system S is given as:

$$y = \frac{1}{2} \ln \frac{1 + \beta}{1 - \beta} + \frac{1}{2} \ln \frac{E' + p'_z}{E' - p'_z} \quad (18)$$

The pseudorapidity η characterizes the angle relative to the beam axis and is defined as

$$\eta = -\ln \left(\tan \left(\frac{\theta}{2} \right) \right) \quad (19)$$

where θ is the angle between the beam axis and the Four-vector of the particle.

Using trigonometric functions, exponential functions and introducing the transverse mass $m_T =$

$\sqrt{m^2 + p_T^2}$, one obtains the following relations:

$$\begin{aligned}
 E &= m_T \cdot \cosh y \\
 p_L &= m_T \cdot \sinh y \\
 p &= p_T \cdot \cosh \eta \\
 p_L &= p_T \cdot \sinh \eta
 \end{aligned}
 \tag{20}$$

Exact calculations can be found in appendix section 6.1.

1.4 ALICE publication

On August 24 2021, the ALICE collaboration published their results of the J/Ψ yield and average transverse momenta in p-Pb collisions at $\sqrt{s_{NN}} = 8.16 \text{ TeV}$, recorded in 2016 at the Large Hadron Collider (LHC) at the european center of nuclear research (CERN), Switzerland [16]. It is based on the PhD thesis of Jana Crkovska where she studied the J/Ψ production at p-p collisions and the J/Ψ production multiplicity dependence [3].

The ALICE (A Large Ion Collider Experiment) detector is 16 m high, 26 m long and 16 m wide and is placed at a depth of 56 m under the ground [17]. It consists of several cylindrical subdetectors. The innermost is the inner tracking system (ITS) which reaches from 3.9 cm up to 43 cm distance from the beam line. It includes Silicon Pixel Detectors (SPD) that cover the range $|\eta| < 0.9$. It is used for primary and secondary vertices reconstruction, particle identification and tracking [18].

The Time Projection Chamber (TPC) follows. It consists of a gas filled cylinder with a central electrode. The signal comes from ionisation of the gas by charged particles traversing it. It is the main tracking and particle identification detector of ALICE [19].

The Transition Radiation Detector (TRD) can identify positrons e^+ and electrons e^- . The working principle is based on transition radiation which occurs when a charged particle passes the boundary between two mediums with different dielectric constant [20].

Further detectors are the time-of-flight and EMCAL for particle identification and jet measurements.

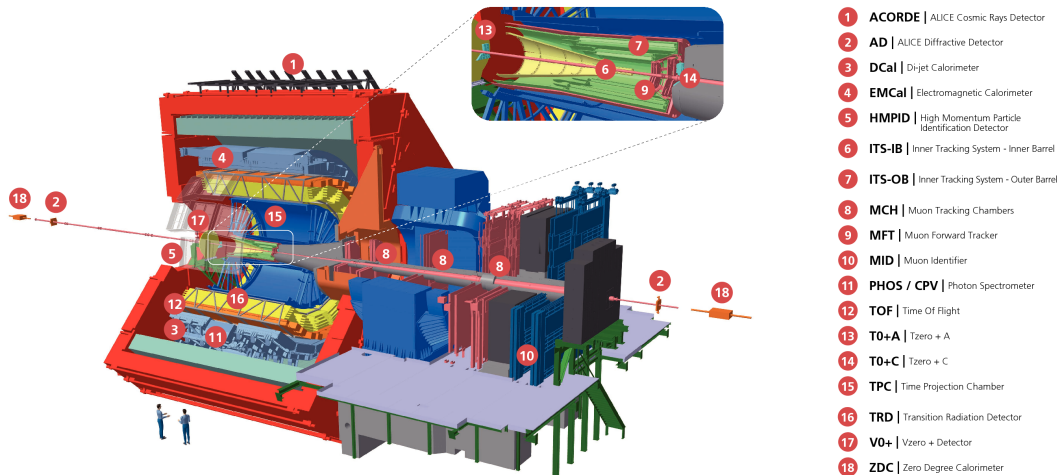


Figure 4: Run 3 ALICE detector after upgrades [21].

For the analysis, the muon spectrometer, silicon pixel detectors, V0 scintillator arrays and neutron Zero Degree Calorimeter (ZDC) of the ALICE detector were relevant [16].

The former is specialized for detecting heavy quark resonances, like the J/Ψ or the bottomonium

Υ by observing the $\mu^+\mu^-$ decay channel. The detectors acceptance is $-4.0 < \eta < -2.5$ [22]. The V0 scintillator consists of the V0A whose acceptance is $2.8 \leq \eta \leq 5.1$ and the V0C with an acceptance of $-3.7 \leq \eta \leq -1.7$. They are each an array of 32 scintillating counters [23]. They are used for online triggers and for avoiding contamination from beam gas events [16]. The ZDC is a set of two detectors on each end of the ALICE detector where each set has a proton and a neutron ZDC [24]. They are used to reject electromagnetic interactions and background [16].

As described before, the J/Ψ production is modified when a QGP is formed. This modification has already been observed experimentally in nucleus-nucleus collisions. Proton-nucleus collisions have also been taken into account to decide whether this effect results from the QGP or from so called cold nuclear matter effects. The measurements reported in reference [16] intend to complement the previously done measurements.

The results for the J/Ψ yield as a function of the normalized charged-particle pseudorapidity density are shown in figure 5. The blue markers indicate the measurement in p-going direction which is towards the muon spectrometer, covering the rapidity interval $2.03 < y_{cms} < 3.53$. The Pb-going direction, represented by red markers, covers the interval $-4.46 < y_{cms} < -2.96$. Even though the yield is in both cases increasing with increasing multiplicity, the growth happens at a different rate. The yield in Pb-going direction increases faster than linear with slope one while the yield in p-going direction, meaning the proton moves towards the Muon spectrometer, grows more slowly. In this thesis, a simulation was made in order to explain this behaviour.

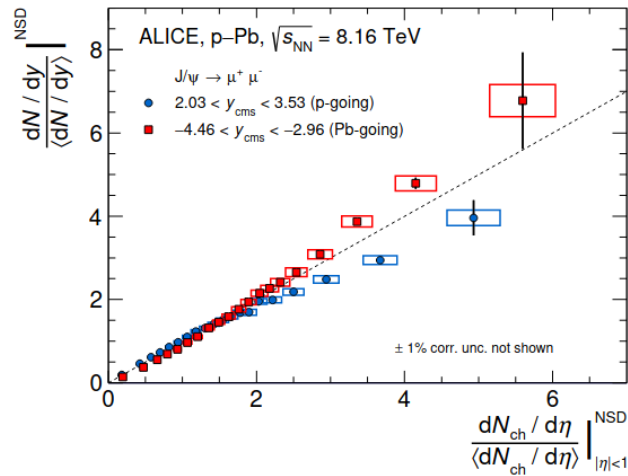


Figure 5: Normalized J/Ψ yield as a function of the normalized charged-particle pseudorapidity density. Blue dots indicate the proton going in negative z direction. Red squares indicate the proton going in positive z direction. Dotted line represents one-to-one-correlation [16].

The mean transverse momentum $\langle p_T \rangle$ dependent on the relative charged particle pseudorapidity density was also measured and presented in figure 6. Throughout the whole multiplicity range, the $\langle p_T \rangle$ measured in the positive y_{cms} interval is above the one measured in negative y_{cms} direction. This also holds true for the multiplicity-integrated value and is consistent with measurements in p-p collisions. At high multiplicities, a $\langle p_T \rangle$ saturation can be seen in both intervals.

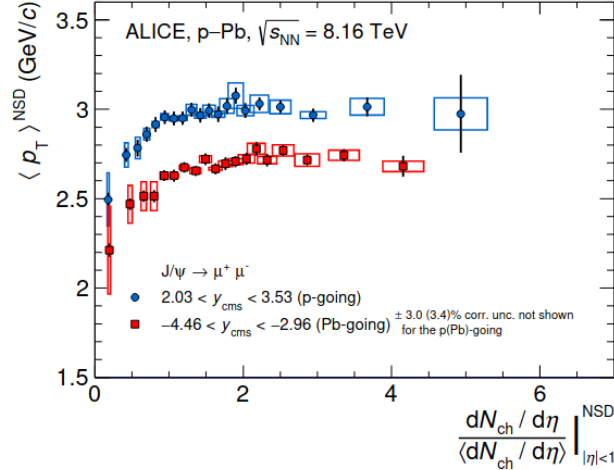


Figure 6: Mean transverse momentum $\langle p_T \rangle$ dependent on the relative charged particle pseudorapidity density. Blue dots indicate the proton going in negative z direction. Red squares indicate the proton going in positive z direction [16].

The measurements presented in figure 5 and 6 were also performed at $\sqrt{s_{NN}} = 5.02$ TeV and agree with the ones at $\sqrt{s_{NN}} = 8.16$ TeV. At $\sqrt{s_{NN}} = 8.16$ TeV, a higher precision was reached and the multiplicity coverage was extended.

It was suggested that the seen behaviour could come from an incoherent superposition of parton-parton collisions where effects vary with rapidity but rather not with the collision energy. [16]

In this thesis it is examined whether this behaviour could also result from acceptance effects in combination with a shift in the center-of-mass system.

1.5 Structure

As a part of this Bachelors thesis, a Glauber Monte Carlo simulation has been written. The first step was to model the lead nucleus by generating single nucleons at different, randomized positions and then calculating the transverse distance to the proton. It was decided whether a collision happened and therefore the number of participants N_{part} was determined which is described in section 2.1.

Then, the p-Pb collision was assumed to be multiple single proton-nucleon collisions in which each charged particles are generated. The number of charged particles N_{ch} was sampled from an extra- and interpolation of given data.

The next step was to reconstruct the pseudorapidity distribution from p-Pb measurements at different centralities. This was done by fitting three boost parameters to η distributions measured in p-p collisions at four different energies. Then, the single proton-nucleon collisions were looked at and the boost parameters were chosen depending on the energy. The single pseudorapidity distributions generated at each collision were added. Since this was not sufficient to describe the data, the proton energy in each collision was decreased. The energy loss was described by different functions as can be seen in section 3.3.

Finally, all steps were connected into the main simulation. The results obtained after some adjustments are presented in section 4.

There was also made a different approach to simulate the given data. The lead nucleus was regarded as a massive target instead of single pp collisions as before.

Both models will be compared and a conclusion will be drawn.

2 Glauber Monte Carlo simulation

Monte Carlo simulations are often used in physics, but they are also used to assess risks for stock prices, project management or pricing. This method was developed in World War II by John von Neumann and Stanislaw Ulam. The difference to other models is that there aren't just fixed inputs but also randomly sampled inputs so that a large number of likely outcomes is produced [25].

The Glauber model was introduced by Roy Glauber. It is used to predict the number of participants and binary collisions depending on the impact parameter b in nuclei collisions. The impact parameter corresponds to the transverse distance of the nuclei colliding, measured from center-to-center [26]. The number of participants can also be calculated analytically by taking the nuclear overlap functions into account.

For this thesis, the ROOT framework was used. It was developed at CERN and is mainly used in high energy physics [27]. Here it was written in C++.

2.1 Simulation of p-Pb collisions

The first step for simulating the proton lead collision by the Glauber Monte Carlo approach was to generate the lead nucleus. It consists of 208 nucleons for which each a position in polar coordinates was modeled. The azimuthal angle ϕ was generated in an evenly distributed range between 0 and 2π using the `TRandom` class and the function `Rndm()`. The polar angle θ was generated in a range between 0 and π . This time, the values were distributed with a sine function. This prevents oversampling on the poles of the sphere. According to the Woods-Saxon distribution, the nucleon density ρ in a nucleus, depending on the radial distance r , is described by

$$\rho(r) = \frac{\rho_0 (1 + wr^2/R^2)}{1 + \exp((r - R)/a)} \quad (21)$$

where w is the so called wine bottle parameter, R the radius of the nucleus and a characterizes the width of the slope. For these Woods-Saxon parameters, there are several values as seen in table 3. The corresponding graphs can be seen in figure 7 where the red function shows the Woods-Saxon distribution using the old parameters and the blue function uses the new parameters. The new values include the deformation of the nucleus and the finite size of the nucleons.

	R (fm)	a (fm)	w
Old	6.62	0.546	0
New	6.66	0.45	0

Table 3: Woods-Saxon parameters for ^{208}Pb [28].

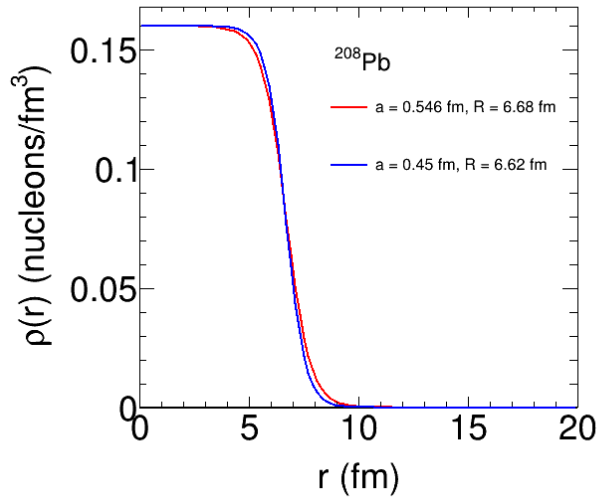


Figure 7: Comparison of Woods-Saxon density distributions for ^{208}Pb with different parameters with $\rho_0 = 0.16$ nucleons/ fm^3 .

A vector with two entries was generated. The first one is containing the position of the proton. The second entry carries the position vectors of all the 208 lead nucleons. After generating each nucleon, the distance to all other nucleons was calculated using a three dimensional pythagoras to make sure that there are no nucleons sitting on top of each other. If their distance was smaller than a specific expulsion distance d_{exp} , the nucleon was deleted and newly generated. According to reference [29], the expulsion distance was $d_{exp} = 0.9$ fm while J. Adam et al. suggest $d_{exp} = 0.4$ fm [30].

The proton was generated at the position $r = \theta = \phi = 0$. Both the proton and the lead nucleus were shifted about half the impact parameter b in opposite directions. The impact parameter b was sampled from

$$f(x) = 2\pi x \quad (22)$$

since it is more probable to hit the outer part of the nucleus than the exact center due to the bigger circumference.

2.2 Collision profiles

After generating all nucleons, the transverse distance d_T between the proton and every lead nucleon was calculated. If the position of the proton is given by (x_p, y_p, z_p) and the position of one lead nucleon is given by (x_n, y_n, z_n) , the transverse distance is:

$$d_T = \sqrt{(x_p - x_n)^2 + (y_p - y_n)^2} \quad (23)$$

In this model, it was assumed that the proton passes the lead nucleus in a straight line without changing its direction after colliding with the lead nucleons. To determine whether a collision takes place or not, there are two models:

The first one is called the hard sphere model and is mostly used in Glauber Monte Carlo simulations. The hit probability p as a function of the impact parameter b is then given by a step function (Figure 8, dotted line):

$$p(b) = \Theta(R - b) \quad (24)$$

In that case the collision probability is always 1 if the calculated distance d_T is below a specific value R . This was calculated from the cross section using equation 16.

The second model is the realistic profile, where the probability $p(b)$ is given by a single Gaussian function:

$$p(b) = A \cdot e^{-\pi A b^2 / \sigma_{in}^{NN}} \quad (25)$$

For this reason it is also known as Gaussian profile. The parameter A depends on the collision energy and was set to $A = 0.92$ [29].

The differentiation between these two models was made because studies have shown, that in the wounded nucleon model some parameters might differ depending on the profile. It influences the eccentricity parameters ϵ^* and higher rank parameters ϵ_n^* as well as the multiplicity fluctuations [29].

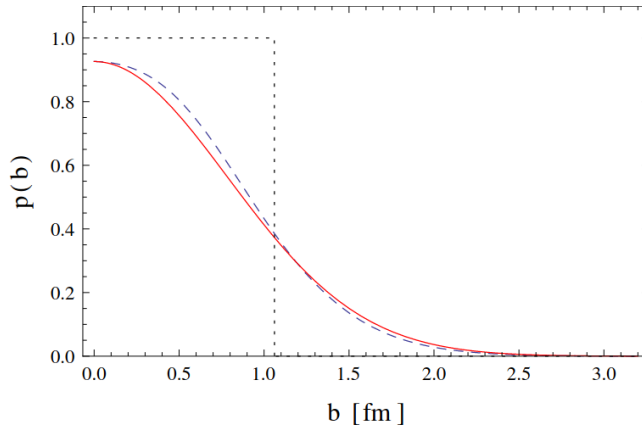


Figure 8: Collision probability as a function of the impact parameter according to different collision profiles. Dotted line indicates the hard sphere model. Red solid line indicates Gaussian profile as in equation 25. Dashed line shows a fit from another reference [29].

If, after these conditions, a collision takes place, the counter of the number of binary collisions N_{coll} raises by one. For the number of participants N_{part} , a second vector with two entries was generated. Again, the first one stands for the proton, while the second entry contains a vector of length 208. Every entry is set to 0. If a particle is involved in a collision, its entry is set to 1. After examining all possible collisions, the entries of the vector are added in order to obtain N_{part} . This whole procedure was repeated with many varying impact parameters.

2.3 Results from the Glauber simulation

Using the ROOT class `TEveGeoShape` and `TGeoSphere`, a 3 dimensional graphic of the nucleons for $b = 0$ was plotted. The hard sphere profile with $\sigma = 70 \text{ fm}^2$ and expulsion distance $d_{exp} = 0.4 \text{ fm}$ were used to obtain the graphic shown in figure 9. The Woods Saxon parameters were $a = 0.546 \text{ fm}$, $R = 6.62 \text{ fm}$. Blue spheres represent the spectators, meaning nucleons that do not take part in the collision, while green spheres represent the participants.

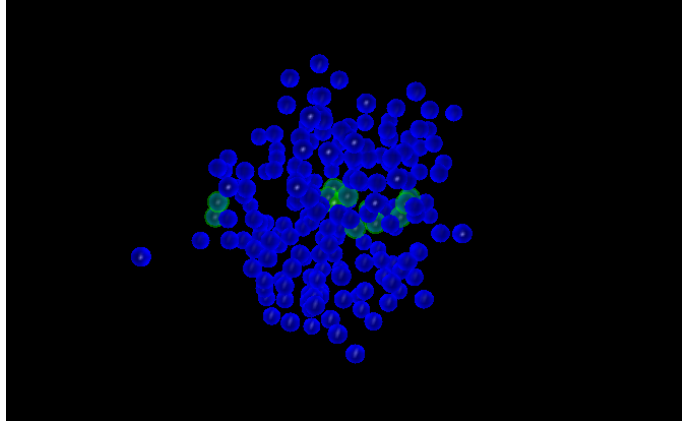


Figure 9: 3D graphic of the lead nucleus colliding with a proton. Blue spheres indicate spectators, green spheres indicate participants of the collision.

To reassure that the positions of the nucleons were generated correctly, the positions in different planes before shifting by b have been plotted in 2D histograms (figure 10). As expected, they all look almost the same since there was no favoured direction in the position generation. Here again can be seen that collisions at for example $b = 10$ fm can take place.

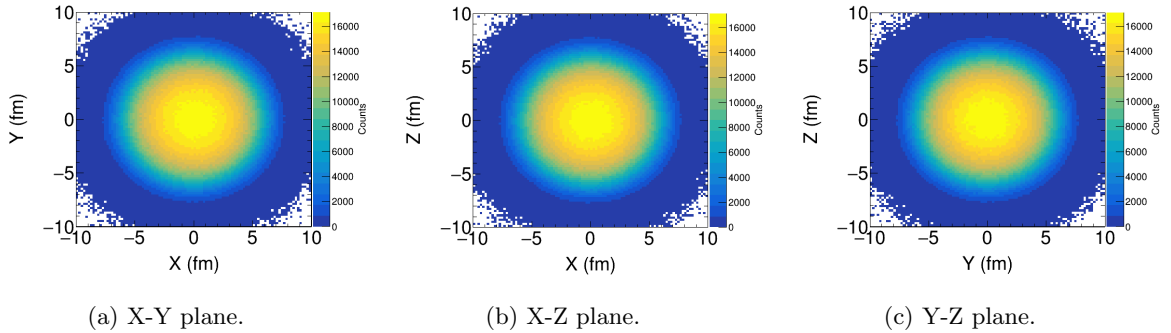


Figure 10: Nucleon distribution in different planes of the lead nucleus.

The number of participants and collisions depending on the impact parameter are shown in figure 11. The figure shows the result of using the same parameters as in figure 9 but with 10000 events and the impact parameter was sampled 100 times. A `TProfile` was also created to show the mean N_{part} , respectively N_{coll} , at every X bin and is plotted in red. As expected, the number of collisions and participants decreases with increasing impact parameter. It is also visible that the number of collisions is by 1 smaller than the number of participants as was foreseeable. The gap at $N_{part} = 1$ in figure 11a results from the fact that there can't be a collision with only one participant. It is also interesting to see that even at $b = 8$ fm which is bigger than the lead ion radius $R = 6.62$ fm, collisions take place. A reason for that is that the Woods-Saxon distribution is not a step function leading to values greater than R being obtainable. The chosen cross section is also relevant for this effect. It is also clearly visible that peripheral collisions are more likely than central collisions.

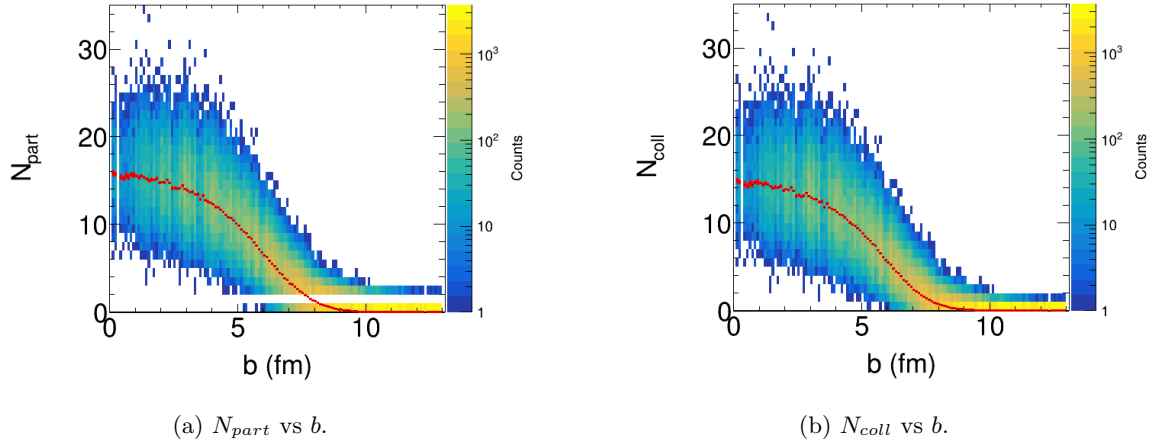
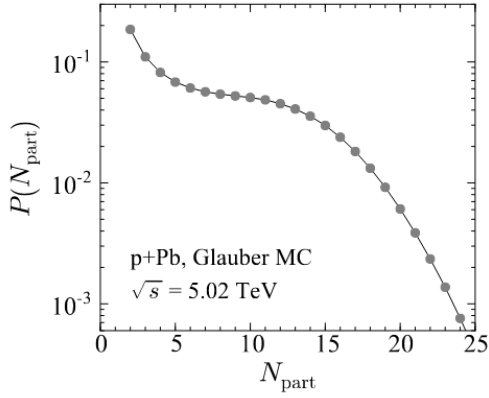
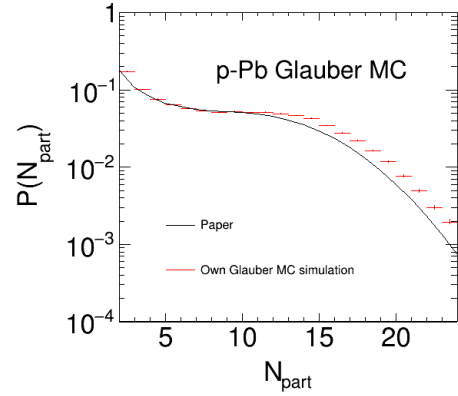


Figure 11: N_{part} and N_{coll} depending on the impact parameter b for the hard sphere profile with $\sigma = 70 \text{ fm}^2$ and $d_{exp} = 0.4 \text{ fm}$. A profile shows the mean values in red.

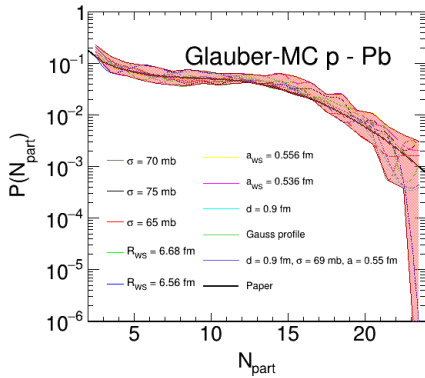
Furthermore, the probability distribution of the number of participants was plotted and compared to a published distribution that can be seen in figure 12a [31]. The latter was obtained by a standard Monte Carlo Glauber approach with a Gaussian profile and $\sigma = 70 \text{ mb}$, simulating a p-Pb collision at $\sqrt{s} = 5.02 \text{ TeV}$. The parameters, namely σ , d_{ext} , a , R and the collision profile of the simulation made in this thesis were varied to study the systematics. The Woods-Saxon parameters were varied within the interval of the old and new values shown in table 3. Then it was also switched between the Gaussian and hard sphere profile and the two expulsion distances $d_{ext} = 0.9 \text{ fm}$ and $d_{ext} = 0.4 \text{ fm}$. The cross section was varied in an interval of 65 to 75 mb. In figure 12b, the N_{part} distribution for the same parameters as before but with 2000 events and 70 impact parameters is shown. In figure 12c, various N_{part} distributions can be seen. An errorband which involves all distributions was also plotted. The mean value was also calculated and can be seen in figure 12d.



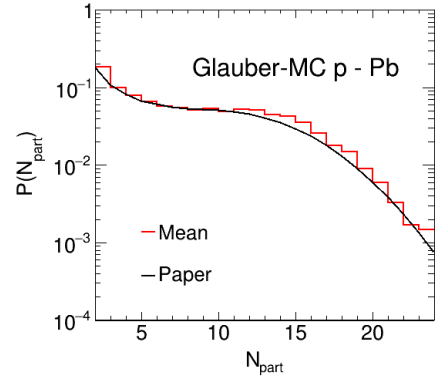
(a) N_{part} distribution [31].



(b) N_{part} distribution at certain parameters.



(c) N_{part} distribution at varying parameters.



(d) Mean of N_{part} distributions.

Figure 12: N_{part} probability distributions. Upper: Left from [31], on the right from our own Glauber Monte Carlo simulation with certain parameters. Lower: Left with varying parameters, the mean of these distributions is shown on the right.

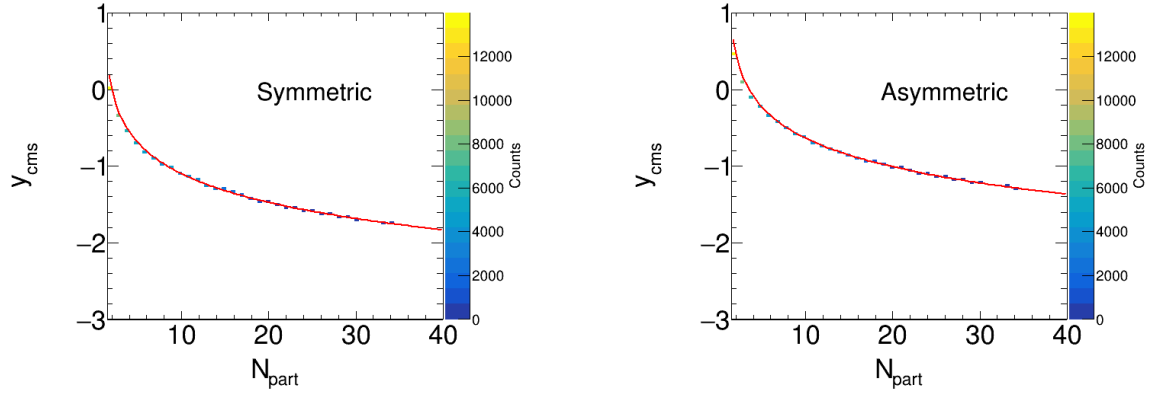
The rapidity was also investigated. For this, a function was written using the ROOT class `TLorentzVector` which allows to set four-vectors. If an energy per nucleon $E_n = 2760$ GeV is given, then the proton has the energy $E_p = E_n$ while the nucleons, that the proton is colliding with, will have $E_{Pb} = E_n \cdot (N_{part} - 1)$ for the assumption that the proton interacts with all participating nucleons at once. The momenta can be calculated using equation 9 and the proton mass $m_p = 0.938$ GeV:

$$\begin{aligned}
 p_p &= \sqrt{E_p^2 - m_p^2} \\
 p_{Pb} &= -\sqrt{E_{Pb}^2 - ((N_{part} - 1)m_p)^2}
 \end{aligned}
 \tag{26}$$

The opposite sign results from the particles moving towards each other in order to collide. The four-vectors can then be set to $p_p^\mu = (0, 0, p_p, E_p)$ and $p_{Pb}^\mu = (0, 0, p_{Pb}, E_{Pb})$. The rapidity is then given by using the function `Rapidity()` on the sum of the two four-vectors. The result can be seen in figure 13a. It decreases monotonically with increasing N_{part} and is equal to or smaller than 0 which is expected due to the energetic asymmetry towards the in negative direction going lead nucleons.

In the analysis, the particle beams won't start of with the same energy per nucleon but with $E_p = 4000$ GeV and for a lead nucleon $E_{Pb}^n = 1580$ GeV. In this case the first collision with

$N_{part} = 2$ has a higher proton energy than lead energy which is the reason why y_{cms} tends to the proton going (positive) direction. Therefore $y_{cms} > 0$ but from $N_{part} = 4$ on the energetic asymmetry shifts towards the negative going direction. The behaviour can be seen in figure 13b.



(a) Symmetric energy per nucleon
 $E_n = 2760$ GeV.

(b) Asymmetric energies per nucleon
 $E_p = 4000$ GeV and $E_{Pb}^n = 1580$ GeV.

Figure 13: Rapidity y_{cms} as a function of N_{part} . Red solid line: Analytic calculation. Histograms are from Glauber simulation.

3 Multiple collision model

In this thesis the proton lead collision is assumed to consist of multiple consecutive proton-nucleon collisions. For this reason, data from p-p collisions can be used for the simulation. A similar approach was already made in 1997 based on S-S and Pb-Pb collisions and is called the LEXUS model which stands for linear extrapolation of ultrarelativistic nucleon-nucleon scattering. A Glauber simulation was used in order to simulate a nucleus-nucleus collision as a sequence of binary nucleon-nucleon collisions [32]. From this model on it was examined whether the multiplicity in Pb-Pb collisions can be reproduced using p-p data. By comparing the results of this model to measured Pb-multiplicities, the stopping mechanism of the nucleons was quantified by assuming that there is a constant change in the rapidity [33].

In a second approach the participating nucleons are considered as a massive target which will be further described in section 4.4.

3.1 First steps

The very first step is to set the direction of the proton and lead nucleus. In the first run, the variable *sign* is set to +1 and in the second run, it is set to -1. Then an event loop was created. In this loop the number of participants is determined from the N_{part} distribution created in section 2 by using the function `GetRandom()` which picks a random number by regarding the function shape. From this the number of binary collisions $N_{bin} = N_{part} - 1$ can be determined easily. A counter for the total number of charged particles is set to 0. Then a loop over each binary collision is created where the proton energy is set. This step is looked more into in section 3.3.

Knowing the proton mass m_p , energy E_p and the lead nucleon energy $E_{Pb}^n = 1580$ GeV, a `TLorentzVector` for each the proton and the lead nucleon can be set: $p_p^\mu = (0, 0, sign \cdot p_p, E_p)$ and $p_{Pb}^\mu = (0, 0, -sign \cdot p_{Pb}, E_{Pb})$. By applying equation 11 the total center-of-mass energy \sqrt{s} was calculated.

3.2 Generation of charged particles

The next step was to determine the number of charged particles N_{ch} . The first attempt was to reproduce the N_{ch}/N_{part} vs N_{part} distribution (figure 15a) from a Monte Carlo simulation of p-Pb collisions at $\sqrt{s} = 5.02$ TeV [30], more precisely the V0M measurement. It was produced by combining the table 4 with the pseudorapidity distribution in figure 14.

Centrality (%)	$\langle b \rangle$ (fm)	$\langle N_{part} \rangle$
0 - 5	3.12	15.7
5 - 10	3.50	14.0
10 - 20	3.85	12.7
20 - 40	4.54	10.4
40 - 60	5.57	7.42
60 - 80	6.63	4.81
80 - 100	7.51	2.94
0 - 100	5.56	7.87

Table 4: Geometric properties of p-Pb collisions. σ and mean values were obtained using a Glauber Monte Carlo approach [30].

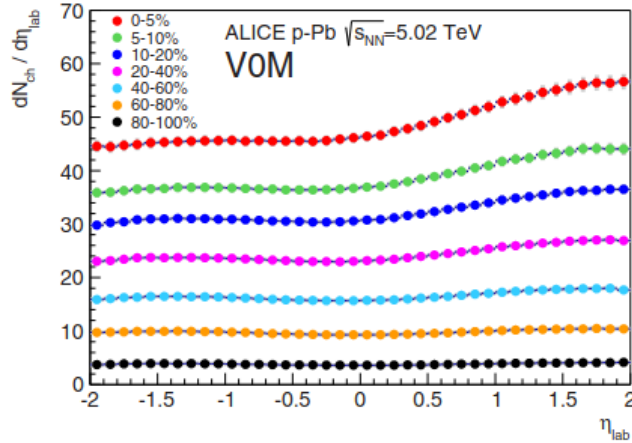
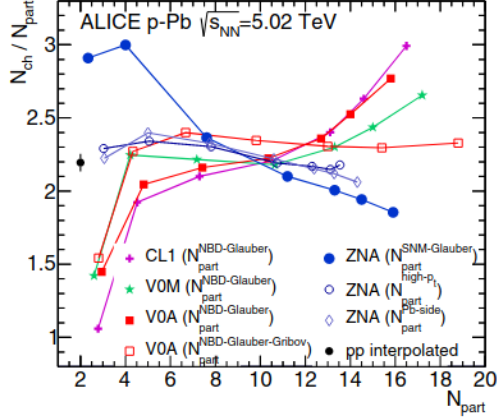


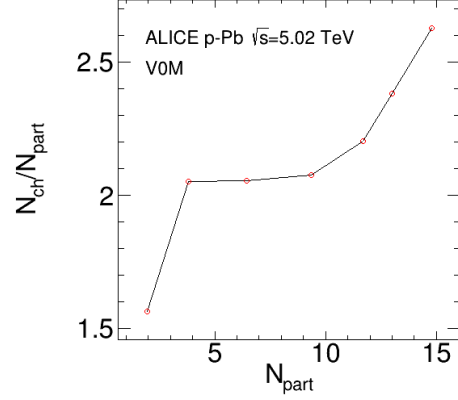
Figure 14: η density distributions for different centrality classes in p-Pb collisions with $\sqrt{s} = 5.02$ TeV [30].

For every centrality interval, the number of charged particles was evaluated at midrapidity from figure 14. Then, it was divided by the corresponding number of participants from the table and a point was set at $x = N_{part}$ and $y = 0.84 \cdot N_{ch}/N_{part}$. The factor of 0.84 comes from the TPC acceptance. The result can be seen in figure 15b.

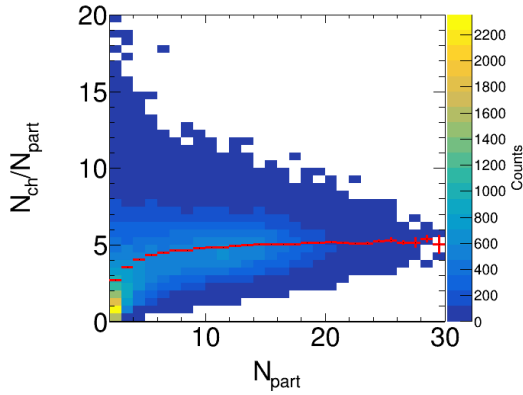
Using the Glauber Monte Carlo simulation described in section 2, it was tried to reproduce this behaviour. For this purpose, at every binary collision a number of charged particles was sampled from the particle multiplicity distribution measured in p-p collisions as shown in figure 17b and they were added. Because of the η range of $|\eta| < 0.8$, the sum of N_{ch} was divided by 1.6 and afterwards divided by $(N_{part} - 1)$. The decision to divide by this divisor and not only by N_{part} stems from that the charged particles result from two participants, not only from one. In a binary collision, only one set of charged particles will be generated even though there are two participants. The result is shown in figure 15d using the same parameters as before but 100 events and 2000 impact parameters. As one would expect $N_{ch}/(N_{part} - 1)$ is constant.



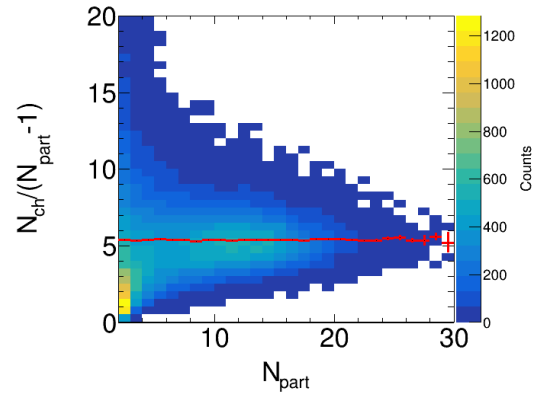
(a) Measured at ALICE in p-Pb collisions at $\sqrt{s} = 5.02$ TeV [30].



(b) Reproduction of figure 15a using η distribution and table 4.



(c) As in figure 15d but with a divisor of N_{part} . TProfile indicated in red.



(d) Distribution generated by Monte Carlo simulation with data from $\sqrt{s} = 7$ TeV p-p collisions. TProfile indicated in red.

Figure 15: Number of charged particles at midrapidity per participant vs N_{part} .

For comparing it to the paper, the same distribution with a divisor of N_{part} has also been done. In this case, the strong increase at low N_{part} can be seen just as in the reference. Nevertheless there is a factor of 2 of difference. It has to be noted that there is an energy difference: In figure 15a it is $\sqrt{s} = 5.02$ TeV while a distribution at $\sqrt{s} = 7$ TeV has been used in the MC simulation to obtain the charged particles. In addition it was assumed that the full energy is available in every collision. For this reason another approach was made after executing the calculations described in section 3.3. In this approach the proton energy decreases with every collision according to equation 37 which leads to less charged particles. The energy dependence of the charged particle multiplicity is depicted in figure 18b. The number of charged particles per $N_{part} - 1$ dependent on N_{part} is shown with this new approach in figure 16b. When there are only two participants, the total center-of-mass energy is highest and therefore the highest number of charged particles is produced. With increasing N_{part} , \sqrt{s} decreases so that less charged particles are produced. Figure 16a shows the same shape as figure 15c but with lower N_{ch}/N_{part} values than before. This was expected because N_{ch} was not sampled from a 7 TeV multiplicity distribution but from lower energies. The starting value at $N_{part} = 2$ which corresponds to a p-p collision has a value of approximately $N_{ch}/N_{part} \approx 2.1$. In figure 15a, a p-p measurement was also depicted as a black point at $N_{ch}/N_{part} \approx 2.2$. With growing N_{part} the distribution in figure 16a shows a saturation

at about $N_{ch}/N_{part} \approx 3.2$. Therefore the difference of a factor of 2 can almost be diminished by taking a decreasing energy into account.

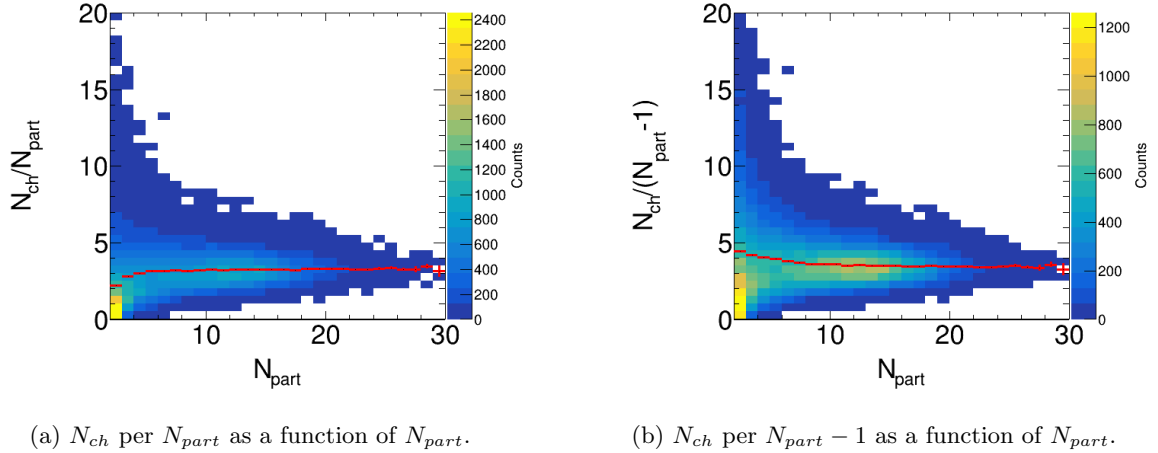


Figure 16: Number of charged particles at midrapidity per participant respectively collision vs N_{part} . Both generated at Glauber Monte Carlo simulation using a decreasing proton energy. TProfile indicated by red markers.

Another attempt to obtain the number of charged particles was to use the probability distributions of N_{ch} at $\sqrt{s} = 0.9 \text{ TeV}$ and $\sqrt{s} = 7 \text{ TeV}$ (figure 17) in order to obtain probability distributions at every energy. The mean numbers $\langle N_{ch} \rangle$ of these two distributions were $\langle N_{ch} \rangle_{0.9 \text{ TeV}} = 5.66/1.6$ and $\langle N_{ch} \rangle_{7 \text{ TeV}} = 8.63/1.6$.

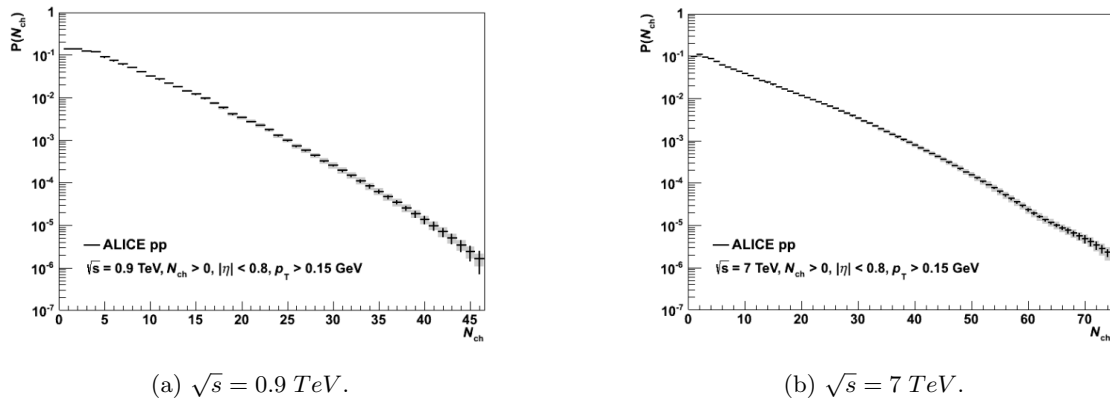


Figure 17: Probability distribution of number of charged particles N_{ch} at different \sqrt{s} [34].

The first approach to interpolate these distributions was to rescale them. For this, the 0.9 TeV distribution was rescaled until it was lying on top of the 7 TeV one. This was found at a factor of $80/45 \approx \langle N_{ch} \rangle_{7 \text{ TeV}} / \langle N_{ch} \rangle_{0.9 \text{ TeV}}$ which was used to rescale the x values. The y values are rescaled in order to normalize the distribution. Then, a 2D histogram was created which shows the probability distribution of the number of charged particles at every energy. The mean N_{ch} at p-p collisions at ALICE shows an $s^{0.11}$ dependency [35], meaning it can be described by a function of the form

$$\langle N_{ch} \rangle = a \cdot \left(\frac{s}{\text{GeV}^2} \right)^{0.11} + b = a \cdot \left(\frac{\sqrt{s}}{\text{GeV}} \right)^{0.22} + b \quad (27)$$

The parameters a and b were varied until the function evaluated at 7 TeV and 0.9 TeV yields the same $\langle N_{ch} \rangle$ as the two distributions. This happened at $a = 0.728$ and $b = 0.288$.

At a given \sqrt{s} , equation 27 was evaluated so that one obtained $\langle N_{ch} \rangle|_{\sqrt{s}}$. Next, the 0.9 TeV distribution was copied and the x values were shifted by a factor of $\langle N_{ch} \rangle|_{0.9 \text{ TeV}} / \langle N_{ch} \rangle|_{\sqrt{s}}$. Then, the integral was calculated for the purpose of dividing the y values by it so that the distribution is normalized. This procedure was repeated but with the 7 TeV distribution instead of the 0.9 TeV one. In that case, the factor was $\langle N_{ch} \rangle|_{7 \text{ TeV}} / \langle N_{ch} \rangle|_{\sqrt{s}}$. This was repeated for every \sqrt{s} . Since now there are 2 distributions at every \sqrt{s} , they need to be combined. The method used was to take the weighted average. The energy interval has a size of 6100 GeV. The goal is that when the energy is for example 6.9 TeV the weight of the 7 TeV distribution is much higher than the one of the 0.9 TeV distribution. Therefore the weight w was calculated as

$$\begin{aligned} w_{7 \text{ TeV}} &= 1 - \frac{(7000 - \sqrt{s}) \text{ GeV}}{6100 \text{ GeV}} \\ w_{0.9 \text{ TeV}} &= 1 - \frac{(\sqrt{s} - 900) \text{ GeV}}{6100 \text{ GeV}} \\ w_{0.9 \text{ TeV}} + w_{7 \text{ TeV}} &= 1 \end{aligned} \quad (28)$$

The y values of the final distribution were then

$$y = w_{7 \text{ TeV}} \cdot y_{7 \text{ TeV}} + w_{0.9 \text{ TeV}} \cdot y_{0.9 \text{ TeV}} \quad (29)$$

The result of this procedure can be seen in figure 18a. The red dots mark the mean N_{ch} from the two given probability distributions. The function 27 was inverted and plotted into the 2D histogram (figure 18a, solid red line). As can be seen, the $\langle N_{ch} \rangle$ from this function and from figure 17 agree.

For this method, the N_{ch} distributions in an interval of 0.9 TeV up to 7 TeV were generated. Since there might also be energies below 0.9 TeV, this is not sufficient for the simulation. Therefore another approach was made using a linear function of the following form.

$$P(\sqrt{s}) = a \cdot \sqrt{s} + b \quad (30)$$

First a 2D histogram was created again with \sqrt{s} on the y axis, N_{ch} on the x axis and $P(N_{ch})$ on the z axis. Then steps with size 1 through the x axis were made. The two given N_{ch} distributions were evaluated at the N_{ch_x} corresponding to the bin so that there are two probabilities $P(N_{ch_x})|_{0.9 \text{ TeV}}$ and $P(N_{ch_x})|_{7 \text{ TeV}}$. Then, the slope a was calculated by dividing the $P(N_{ch})$ difference by the energy difference. The offset b can be calculated by solving equation 30 so that the linear function is given by:

$$P(\sqrt{s}) = \frac{\Delta P(N_{ch_x})}{\Delta \sqrt{s}} \cdot \sqrt{s} + \left(P(N_{ch_x})|_{0.9 \text{ TeV}} - 900 \text{ GeV} \cdot \frac{\Delta P(N_{ch_x})}{\Delta \sqrt{s}} \right) \quad (31)$$

This means that the probability at a specific N_{ch_x} for every \sqrt{s} can be determined. Then it was stepped through the \sqrt{s} bins with a step size of 10 GeV and the linear function was evaluated at every \sqrt{s} so that every bin in the 2D histogram is filled with a probability for N_{ch} . The result of this procedure is given in figure 18b. This is used to make a **ProjectionX** at a given energy to obtain the probability distribution $P(N_{ch})$ that one can sample from.

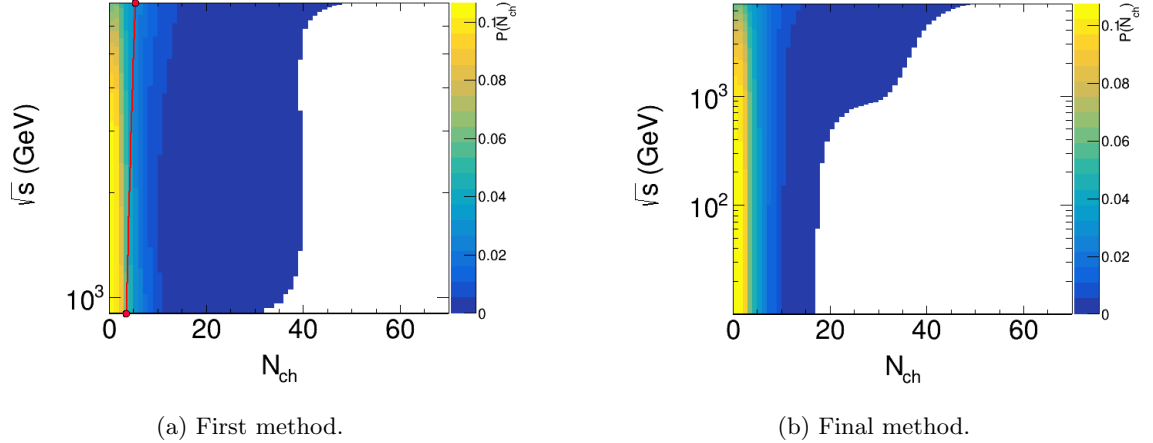


Figure 18: Two dimensional histogram that shows the probability distribution of the number of charged particles at various energies.

After generating N_{ch} , a loop over the charged particles was made. They will be assigned to the J/Ψ mass $m_{J/\Psi} = 3.096916$ GeV and the sign of the direction in which they propagate will be decided randomly. The azimuthal angle ϕ gets sampled in an interval of 0 to 2π . For the polar angle θ , a random value in the interval of -1 to 1 will be assigned to $\cos \theta$ so that θ can be determined by using the inverse trigonometric function. Using equation 19, η can be determined. The transverse momentum of the charged particle is getting sampled where a Levy function was used. It has the following form:

$$f_{\text{Levy}}(x) = A \cdot x^2 \cdot e^{-\frac{\sqrt{x^2 + m_0^2}}{T}} \quad (32)$$

where the amplitude was set to $A = 1.0$ and the mass to $m_0 = 0.1$. Two of these Levy functions were defined, one with $T = 1.5$ GeV and the other with $T = 0.75$ GeV. Then a random number between 0 and 1 was generated and if it is over a certain value (which was called `jet_bulk_pT_fraction`), the function with $T = 0.75$ GeV was used to sample from and in the other case, the $T = 1.5$ GeV function was used. This procedure was done to model a soft and hard p_T component. In figure 19 the p_T spectrum is shown. The black markers indicate a J/Ψ p_T measurement at ALICE at a p-p collision [36]. The three histograms were created after executing the Bjorken boost but before the center-of-mass boost which are further described in sections 3.3 and 3.4. The red histogram shows the transverse momentum of particles with pseudorapidities below 0.8 and the blue one for rapidities below 0.1. The green one depicts the p_T values within the η acceptance of $-4.0 < \eta < -2.5$.

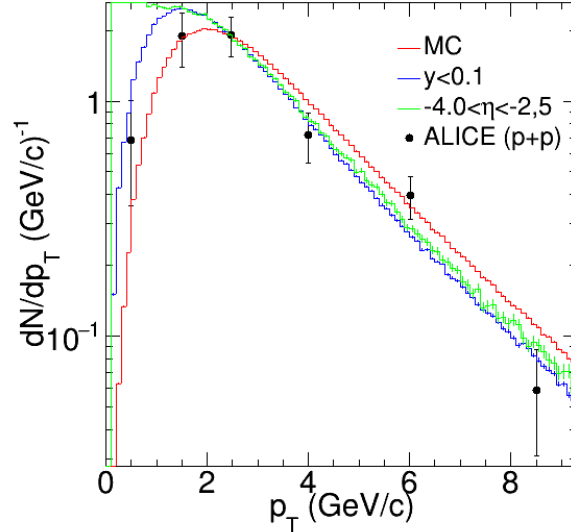


Figure 19: Transverse momentum p_T spectrum of the J/Ψ . Black markers are from p-p ALICE measurement [36].

Knowing the mass $m_{J/\Psi}$, the sampled p_T , the azimuthal angle ϕ and the calculated η , a `TLorentzVector` for the J/Ψ can be set.

3.3 η distribution

The charged particles will then undergo a boost along the beam direction inspired by the Bjorken model of emitting sources which freeze out along the z -axis. In the following, this is called the Bjorken boost. In this model, the two colliding nuclei are regarded as thin discs consisting of nucleons. The thin shape results from Lorentz contraction since the nuclei are assumed to move at velocities near the speed of light. When they collide a fluid forms between the discs as indicated in figure 20. This fluid then expands longitudinally while it is resting at midway between the discs. After the collision, the thin discs recede in opposite directions from the collision point. In this model, a "central plateau" is assumed for the particle production depending on the rapidity so the particle production only depends on the initial energy deposited in the central collision region shortly after colliding [37]. This boost ensures that these effects are taken into account and this results in the pseudorapidity distribution having the desired shape which will be shown in figure 22.

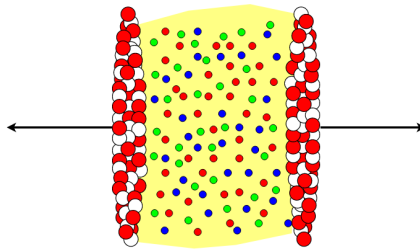


Figure 20: Nuclei after colliding regarded in the Bjorken model [38].

The goal is to optimize the parameters of the boost so that the η distributions in p-Pb collisions

at $\sqrt{s} = 5.02$ TeV were reconstructed as in figure 14. This was done by assuming that the p-Pb collision consisting of $N_{part} - 1$ proton-nucleon collisions yields multiple single p-p η distributions that can then be added. N_{part} differs depending on the centrality as can be seen in table 4. The first step was to reconstruct the η distributions in p-p collisions at four different energies, namely 0.2 TeV, 2.76 TeV, 7 TeV and 13 TeV from figure 21.

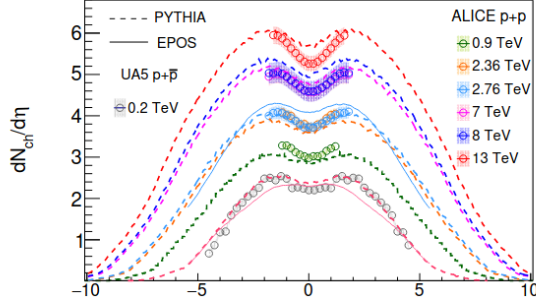


Figure 21: η density distributions in p-p collisions with varying \sqrt{s} [35].

The data points and their continued distribution calculated by PYTHIA have been scanned using the tool `xyscan`. These p-p pseudorapidity distributions are then recreated by writing a simulation. Therein first the number of charged particles in a binary collision was generated by evaluating the graph in figure 15b at $N_{part} = 2$ and multiplying this by $N_{part} = 2$. This gives $N_{ch} = 3.16$. In p-p collisions measured at ALICE, the proton to Pion ratio $(p + \bar{p})/(\pi^+ + \pi^-)$ for $\sqrt{s} > 0.9$ TeV is approximately 0.055 and the Kaon to Pion ratio $(K^+ + K^-)/(\pi^+ + \pi^-)$ is about 0.13 at $\sqrt{s} \approx 7$ TeV [39]. Since the simulation for the η distributions model a p-p collision, the masses of the resulting charged particles have to match these ratios. For this reason, a random number was generated between 0 and 1. If it is smaller than 0.055, the mass of the charged particle is the proton mass $m_p = 0.938$ GeV. If it is greater than or equal to 0.055 and smaller than 0.055+0.13, the mass will be the Kaon mass $m_K = 0.493$ GeV. Otherwise, the mass of the charged particle will be assigned to the Pion mass $m_\pi = 0.139$ GeV.

Next the sign of the direction of the charged particle is decided randomly, the other coordinates are decided as in section 3.2. The transverse momentum p_T is sampled from an inclusive transverse momentum distribution measured at ALICE at $\sqrt{s} = 5.02$ TeV p-p collisions for different centrality classes [40]. Because four p-p η distributions shall be reconstructed, there will be four different Boost vectors which correspond each to an energy. For this reason four equal Lorentz vectors are set which then undergo different Bjorken boosts. This boost consists of several parameters: The width of the Gaussian rapidity w_G^y and the range of the Bjorken rapidity R_B^y . First a random number between 0 and 1 is generated. If it is smaller than the fraction f_{BG}^y , the Bjorken z rapidity is generated as

$$y_B = (ran - 0.5) \cdot R_B^y \quad (33)$$

where ran is a random number between 0 and 1. In the other case, the z rapidity is sampled from a Gaussian with $\mu = 0$ and a standard deviation of $\sigma = w_G^y$. The relation between the rapidity and the longitudinal velocity β_L is shown in equation 17. Therefore β_L can be calculated using the sampled rapidity as

$$\beta_L = \tanh y = \frac{e^{2y} - 1}{e^{2y} + 1} \quad (34)$$

The rapidity boost vector is then set to $(0, 0, \beta_L)$. After boosting the charged particles, their pseudorapidity is filled into a histogram using the function `Eta()`. This procedure was done four times where the three boost parameters were varied manually in order to obtain matching

η distributions at every energy. The scanned data from figure 21 was plotted with the resulting histograms. The three chosen boost parameters depending on the energy are shown in table 5. The corresponding histograms and data can be seen in figure 22b. For every parameter a TGraph was created showing the value of the parameter as a function of \sqrt{s} .

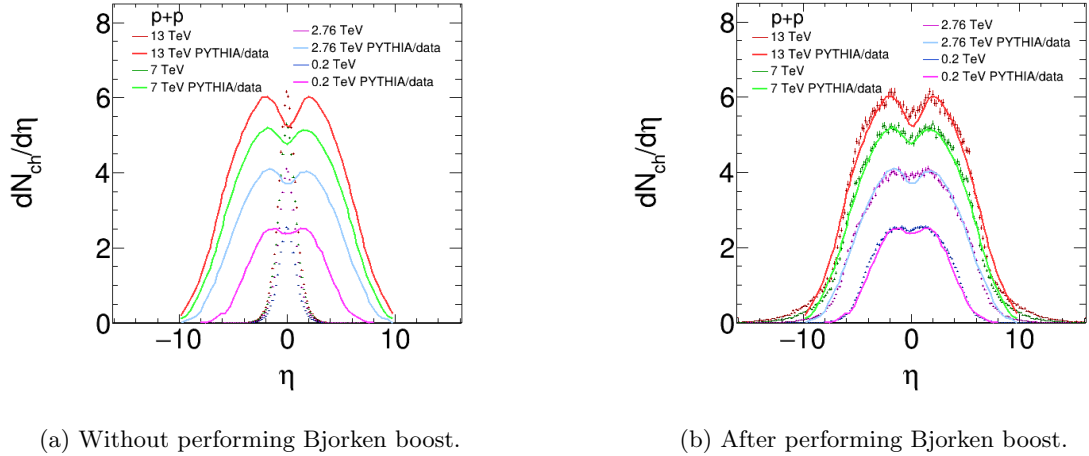


Figure 22: η distributions for various energies before and after performing the Bjorken boost in z direction. Solid lines represent the data from figure 21 [35]. Histograms result from procedure described above.

\sqrt{s} (TeV)	f_{BG}^y	R_B^y	w_G^y
0.2	0.5	9.0	2.5
2.76	0.4	12.0	3.5
7	0.4	12.0	4.2
13	0.45	12.0	4.7

Table 5: Boost parameters at different energies in order to obtain η distributions as in figure 21.

The next step was to go back again to the p-Pb collision. The mean number of participants in a central collision is $\langle N_{part} \rangle = 15.7$ so that a loop over 15 collisions was made. The lead nucleons had an energy of $E_{Pb} = 1580$ GeV while the proton had an initial energy of $E_p = 4000$ GeV. The proton went into negative z direction while the lead nucleus went in positive z direction. Knowing the proton mass and the energy, the momentum can be calculated and therefore the Lorentz vector for the proton and lead nucleon can be set. Then, the two vectors were added for the purpose of creating a center-of-mass boost vector. The total center-of-mass energy was also calculated from the added vectors by using the function `Mag2()`. Knowing \sqrt{s} , the number of charged particles can be determined as seen in section 3.2. For every charged particle, the mass and the Lorentz vector were determined as described in the previous part. The boost parameters were taken from the graphs that show the \sqrt{s} -dependence of the parameters and the particles were boosted. After this rapidity boost, a center-of-mass boost was performed. Then again a pseudorapidity histogram was filled. This was done for every binary collision resulting in $N_{part} - 1 = 15$ η histograms which were then scaled and multiplied by N_{ch} so that the center of the histograms is located at their corresponding N_{ch} . Finally the histograms were added depending on the centrality class. In this case, the centralities 0-5 % and 40-60 % were used. For 0-5 %, the first 14 histograms were added. Then, the 15th histogram was scaled with a factor of 0.7 because there are on average 15.7 participants and added on top of the others. According to table 4, $\langle N_{part} \rangle$ is 7.42 for 40-60 %. For this reason, again the first 6 histograms were added and the 7th one was added with a scale factor

of 0.42 to take the full 7.42 participants and not only 7 into account.

The resulting histograms were then plotted with the data from figure 14. In order to see whether the generated histogram suits the data, the χ^2 was calculated. The uncertainties $\sigma_{0-5\%}$, $\sigma_{40-60\%}$ were taken from the data and divided by 10 because they were not statistical. The graphs had each $N = 42$ points. The histograms were evaluated at the x values of each point from the data. The χ^2 can then be calculated as

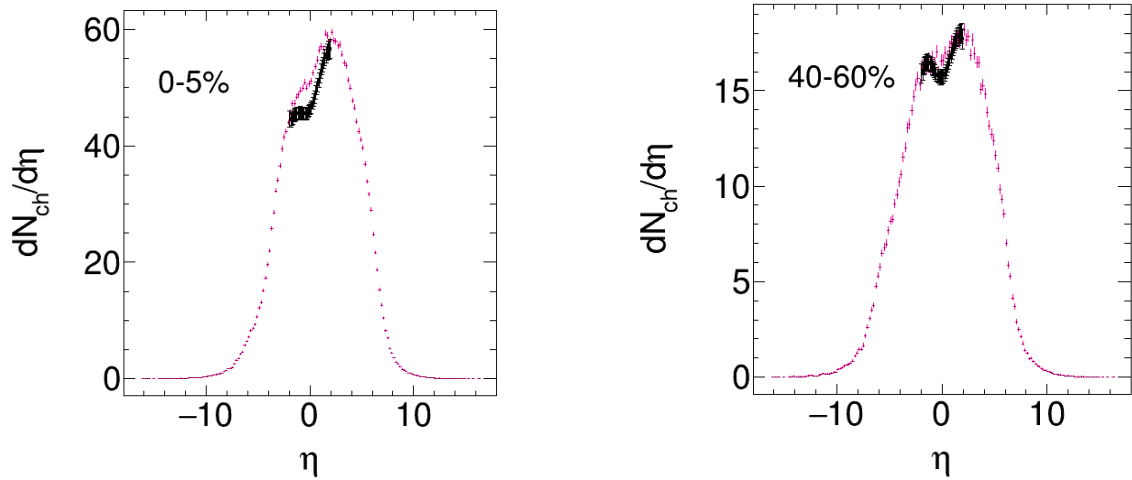
$$\chi^2 = \sum_{i=0}^{N-1} \frac{(y_{0-5\%} - y_{data})^2}{\sigma_{0-5\%}^2} + \sum_{i=0}^{N-1} \frac{(y_{40-60\%} - y_{data})^2}{\sigma_{40-60\%}^2} \quad (35)$$

As shown in figure 14, the more central a collision is, the more asymmetric the distribution is towards the Pb-going direction. In the previously discussed steps this behaviour would not show up because the protons energy is much higher, meaning the asymmetry would appear in the proton going direction. This led to the assumption that the proton energy might decrease with every binary collision. As a first approach, the energy loss was tried to be described by a convolution of an exponential and a linear function:

$$E(x) = a(x - b)e^{c(x-d)} + e \quad (36)$$

Meaning that in the first collision, the proton would have its initial 4000 GeV. In the second collision, the value $E(0)$ would be subtracted from the initial value and in the third collision, $E(1)$ would be subtracted from the energy of the second collision et cetera.

A minimizer `GSLSimAn` was used for the purpose of reaching a minimal χ^2 and therefore the best parameters. For this, some start parameters and their limits have been set. Since there are many parameters it can happen that this function yields strongly negative energies even though some limits are set. This results in unuseful values. For that reason it was set that if the energy undergoes 100 GeV it will be set to $E_p = 100$ GeV. The minimizer yielded the parameters $a = 0.80$ GeV, $b = 0.16$, $c = 0.14$, $d = 70.95$ and $e = 4.28$ GeV. With that the proton energy in the first collision is 4000 GeV just as wanted. In the following collision, it is 1833.74 GeV and from there on 100 GeV.



(a) Centrality 0-5 % corresponding to $N_{part} = 15.7$.

(b) Centrality 40-60 % corresponding to $N_{part} = 7.42$.

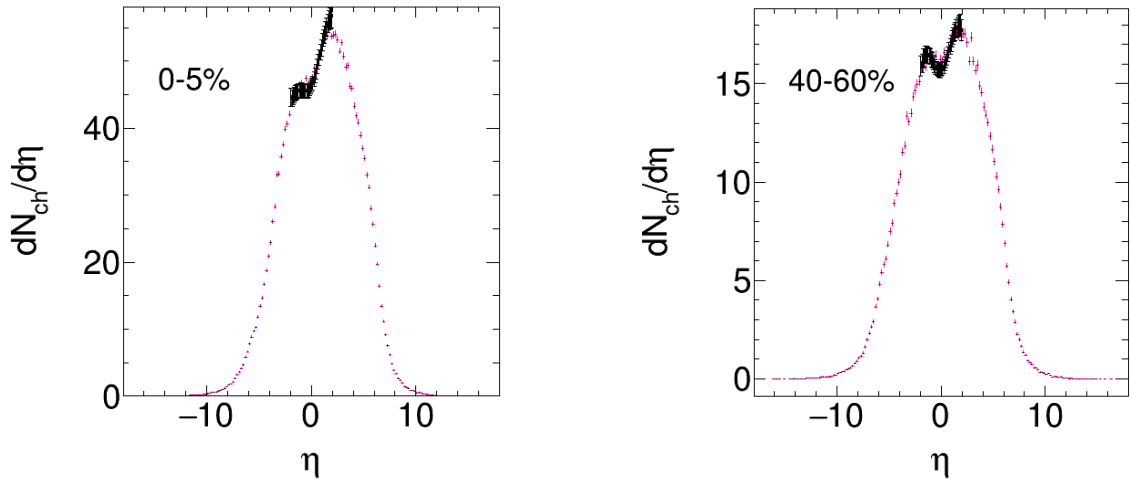
Figure 23: Results of minimizer using convolution (equation 36) to describe energy loss. Data is given in black, added η distributions in pink.

The problem was that this function was not monotonically decreasing. One could have solved this problem by shifting the distribution so that the maximum is at $x = 0$ but instead another function was tried.

The new approach was to describe the energy by

$$E_p = 4000 \text{ GeV} \cdot a^{b \cdot i_{N_{part}}} \quad (37)$$

where $i_{N_{part}}$ is the loop index. The minimizer `GSLSimAn` has been used again and the result with parameters $a = 0.38$ and $b = 0.82$ is shown in figure 24. The χ^2 in this constellation was 5627.02. The large value is due to the previously discussed reduction of the errors by a factor of 10. The fit nicely describes the data.



(a) Centrality 0-5 % corresponding to $N_{part} = 15.7$.

(b) Centrality 40-60 % corresponding to $N_{part} = 7.42$.

Figure 24: Pseudorapidity distributions. In black: Data [30]. In pink: Added histograms from simulation. Energy loss described by equation 37 with parameters $a = 0.38$ and $b = 0.82$.

In figure 21, the circles indicate actual data from ALICE p-p collisions while the dashed lines result from calculations with the PYTHIA model which is a particle production model and the solid lines from the EPOS model. Because of the data one could think that the descent is stronger than indicated from the two models. For this reason, the 0.2 TeV pseudorapidity distribution was scanned again by following the descent that the data points indicate. Then the boost parameters were varied again in order to make an η distribution fitting to the new scanned one. The parameters of equation 37 were newly determined using the new boost parameters and the fitter. They came out as $a = 0.45$ and $b = 0.95$. In contrast to the previous approach, the Bjorken boost parameters are not energy dependent but equal for every \sqrt{s} .

To see the impact of a boost in z direction one can look at figure 26.

To generate this figure, a velocity $\beta = -0.8$ was chosen and for the transverse momentum p_T , 50 values were evenly taken in an interval of 0.1 GeV/c to 7.94 GeV/c. For five values of η which are $\eta = 3.0$, $\eta = 0.0$, $\eta = -1.0$, $\eta = -1.5$, $\eta = -2.0$, a `TGraph` was created each. For every of the 50 p_T values, five `TLorentzVectors` were created using the function `SetPtEtaPhiM()` with the mass $m_{J/\psi}$, $\phi = 0$ and one of the five different η for every of the five vectors. Then these Lorentz vectors were boosted using the boost vector $(0, 0, \beta)$. The x values of the graphs were then set using the function `Eta()` and the y values using `Pt()`. Without boosting there would be a vertical line at each of the five η values which are indicated by the dotted lines in figure 26. After boosting, they are clearly shifted and with increasing η the transverse momentum also increases. The η acceptance is represented by the red sheer box at $-4.0 < \eta < -2.5$.

The longitudinal momentum \vec{p}_L is defined by β and is therefore constant. The p_T values are first small, then increasing. For small p_T values the angle θ between \vec{p}_T and \vec{p}_L is greater than at higher p_T values as indicated in figure 25. Due to the relation between η and θ (equation 19) this leads to higher pseudorapidity shifts at lower transverse momenta.

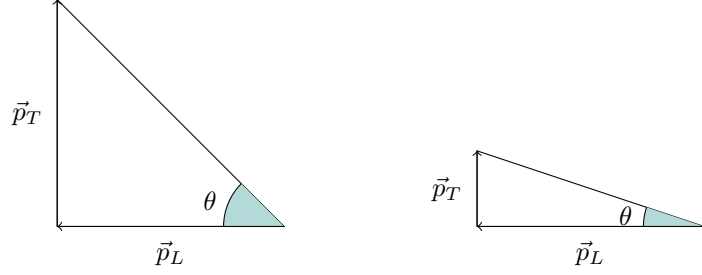


Figure 25: Geometric depiction of the angle dependent on \vec{p}_T for the same \vec{p}_L .

Lower p_T values are therefore more impacted by the boost than higher p_T . This shows that because of the boosting the initial p_T spectrum at mid-rapidity is changed within the Muon spectrometer acceptance.

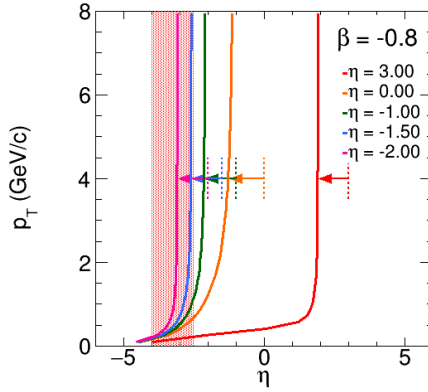


Figure 26: Transverse momentum vs. pseudorapidity after undergoing a boost in z-direction with $\beta = -0.8$. Red sheer box indicates the detector acceptance $-4.0 < \eta < -2.5$. Dotted lines indicate the multiple initial η values.

3.4 Applying the boost

After the parameters of the Bjorken boost were determined, the J/Ψ particles were boosted. Next the Lorentz vectors of the proton and the lead nucleus are added in order to create a boost vector. This boost is necessary because it takes the center-of-mass into account. Due to the decreasing energy of the proton, the center-of-mass shifts from the proton towards the lead nucleus.

Finally the same quantities as shown in section 1.4 are depicted meaning the J/Ψ yield and the mean transverse momentum $\langle p_T \rangle$ as a function of the normalized charged particle pseudorapidity density. For the J/Ψ yield, the number of charged particles which had a transverse momentum higher than 0.1 GeV/c and which were within the detector acceptance, meaning $-4.0 < \eta < -2.5$, was counted. In addition a histogram which shows the transverse momentum p_T as a function of the pseudorapidity η is created. This was done to reassure that there is a splitting happening in the transverse momentum and to see whether the p_T distribution measured in the Pb \rightarrow p direction is above the one of the opposite direction. To calculate the normalized charged particle pseudorapidity density, the number of charged particles in each event was saved. It was then divided by the mean number of charged particles, meaning the total number of charged particles divided by the number of events.

4 Results

In this section the results from the previously discussed steps are presented using 1000000 events. The Bjorken boost parameters were $f_{BG}^y = 0.85$, $R_B^y = 7.5$ and $w_G^y = 1.7$.

4.1 $p_T - \eta$ distributions

With the settings mentioned above, the two dimensional histogram of the transverse momentum as a function of the pseudorapidity η in p→Pb direction is shown in figure 27 where the mean values were calculated using the `TProfile` class and are indicated in black. These were then mirrored at $\eta = 0$ and plotted in red. The red sheer box indicates the η acceptance of the detector. Within this acceptance the black distribution measured in Pb-going direction is above the red distribution which indicates the p-going direction which is not the case for the actual data. It turns out that the distribution is by far too wide which might be a result of using the PYTHIA extrapolations for adjustments. By manually changing the width of the distribution, by multiplying an additional factor, a much better agreement with the data could be achieved.

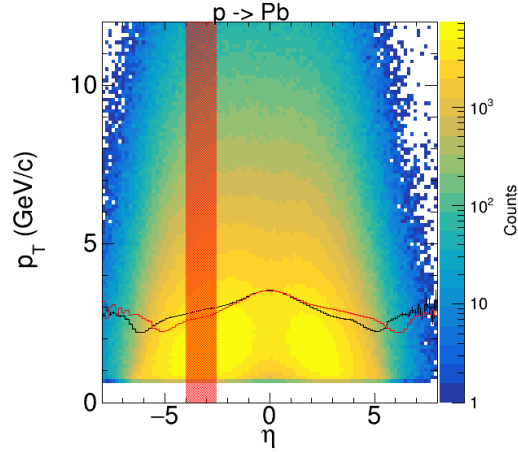
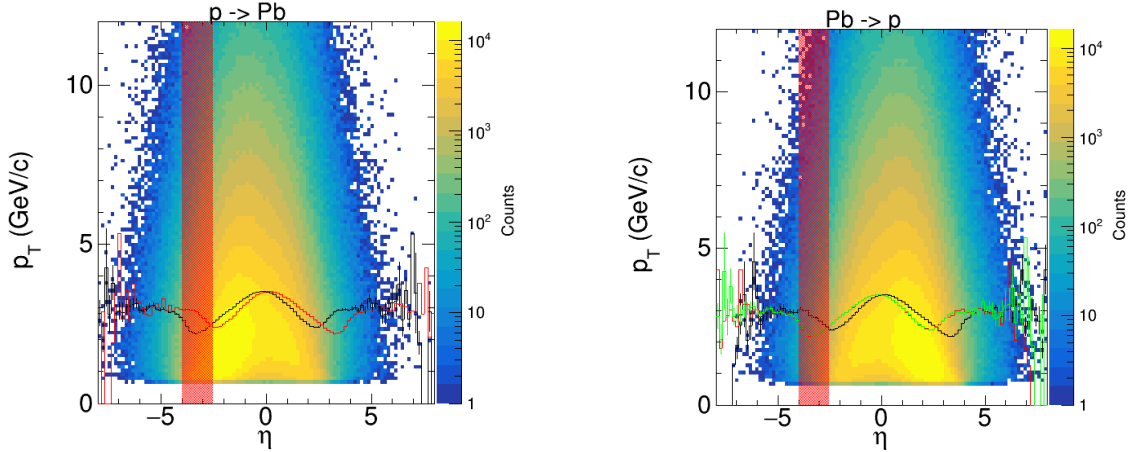


Figure 27: Transverse momentum p_T vs pseudorapidity η as a two dimensional histogram for every N_{part} measured in p→Pb direction. Red sheer box indicates detector acceptance. Black histogram represents mean values. Red histogram result from mirroring the black histogram at $\eta = 0$.

The $p_T - \eta$ distributions in both directions after this alteration using a factor of 0.25 are shown in figure 28. In figure 28b, there is a green histogram which is the `TProfile` of the proton going direction. This was added in order to see whether the mirrored histogram corresponds to the histogram of the other going direction. This seems to be true at least for the pseudorapidity range covered by the detector. Therefore one can already see that there is a splitting in the transverse momentum.

The width of this distribution has a significant effect on the p_T values. When using the energy dependent Bjorken boost parameters, the η distribution is much wider which led the p_T distribution measured in p→Pb direction to be higher than the Pb→p distribution within the acceptance.



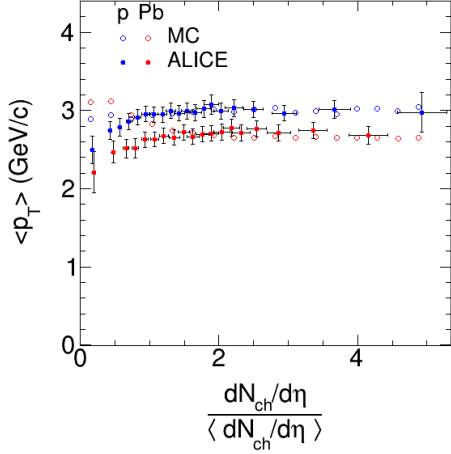
(a) Pb-going direction (sign +1).

(b) p-going direction (sign -1). Green histogram is the profile from the lead going direction.

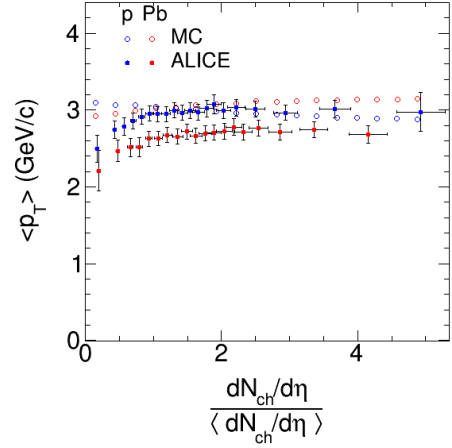
Figure 28: Transverse momentum p_T vs pseudorapidity η for every N_{part} . Red sheer box indicates detector acceptance. Black histograms represent mean values. Red histograms result from mirroring the black histograms at $\eta = 0$.

4.2 Mean transverse momentum

In figure 29, the mean transverse momentum $\langle p_T \rangle$ is shown as a function of the charged particle pseudorapidity density. On the right hand side, the distributions were generated without multiplying y_z by 0.25. As discussed before this results in the Pb-going distribution being above the p-going distribution and therefore this does not describe the data correctly. The $\langle p_T \rangle$ distributions after multiplying y_z by 0.25 is shown on the left. The general shape of the distributions resulting from the previously described simulation matches the data. At $dN_{ch}/d\eta > 0.7$, they are almost the same, the splitting is clearly visible and also the gap between the in two opposite direction measured distributions fits the gap of the two published distributions. At lower multiplicities, the $\langle p_T \rangle$ values show a different behaviour than desired: The in Pb-direction measured values indicated in red start off at about 3.1 GeV/c while the values measured in opposite direction are at approximately 2.9 GeV/c. Nevertheless at $dN_{ch}/d\eta \approx 1.9$, the two distributions cross so that they fit the data.



(a) With multiplying y_z by 0.25.



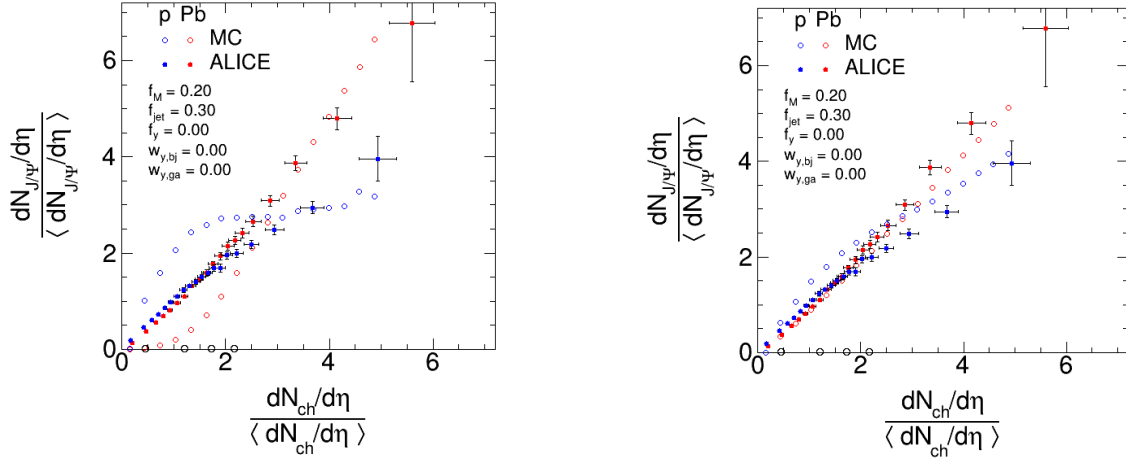
(b) Without multiplying y_z by 0.25.

Figure 29: Mean transverse momentum $\langle p_T \rangle$ versus the normalized charged particle pseudorapidity density. Filled dots indicate ALICE measurement presented in section 1.4. Open markers represent results from the previously presented MC simulation. In both cases, blue represents the p-going direction while red stands for the Pb-going direction.

4.3 J/Ψ yield

The J/Ψ yield as a function of the normalized charged particle multiplicity is shown in figure 30. As before on the right hand side, the distributions without applying the factor of 0.25 are shown. In this case, the general shape matches the data. The gap between the two distributions at high multiplicities is smaller than in the measured distributions. On the left, the result with the factor is shown. The general shape is like measured at ALICE too, meaning that first the yield measured in proton going direction is above the yield measured in the other direction, then the distributions cross so that then the yield in lead going direction is above. In contrast to the ALICE measurement, the crossing does not happen at $dN_{ch}/d\eta \approx 1.6$ but at $dN_{ch}/d\eta \approx 3.9$ which is also true for the distributions without applying the factor. At lower multiplicities the simulated yield values highly differ from the data, for example at $dN_{ch}/d\eta = 1.0$, the yield measured in Pb-going direction is approximately 0.2 and in p-going direction 2.0 while the actual measured value is ≈ 1.0 . At higher multiplicities though the distributions fit the data well.

In general this rather simple model can reproduce the main features that were seen in the p-Pb ALICE data only by performing the boosting and reproducing the emitting source using p-p data with a decreasing proton energy which results in a shift of the center-of-mass system. The overall shape matches the published distributions and even quantitatively, this model yields good results for the $\langle p_T \rangle$ distribution and at higher multiplicities for the J/Ψ yield too. During the analysis it was also visible that the results highly depend on the details of modeling the emitting source. When looking at the $p_T - \eta$ distributions in figure 28 it is also visible that the detectors η acceptance, which is indicated by a red sheer box, plays an important role. If the acceptance would be for example $2.5 < \eta < 4.0$, then the $\langle p_T \rangle$ distributions would be the opposite, meaning that the Pb-going distribution would be above the p-going distribution.



(a) With multiplying y_z by 0.25.

(b) Without multiplying y_z by 0.25.

Figure 30: J/Ψ yield as a function of the normalized charged particle pseudorapidity density. Filled dots indicate ALICE measurement presented in section 1.4. Open markers represent results from the previously presented MC simulation. In both cases, blue represents the p-going direction while red stands for the Pb-going direction.

4.4 Massive target model

In order to explain the behaviour shown in figure 5 and 6 a second approach was made. Here, the collision is visioned as a proton hitting the participating nucleons of the lead nucleus which are regarded as a massive target and not as before as multiple binary collisions.

First the proton momentum p_p was set knowing the proton mass and energy $E_p = 4000$ GeV. The first run was made with the proton going in positive direction so that a `TLorentzVector` could be set as $p_p^\mu = (0, 0, +p_p, E_p)$. Then a number of events $N = 100000$ was chosen and in each event the centrality was sampled in an evenly distributed interval between 0 % and 100 %. Afterwards an initial N_{ch_i} was determined by creating a `TGraph` using the centralities and N_{ch}/η given in the following table and evaluating it at the set centrality. Thereby a spline was created in order to interpolate between the given data points. The outcome was then multiplied by 20.33/17.56 where 20.33 is the averaged charged particle pseudorapidity density at a p-Pb collision with $|\eta| < 1$ [16] and 17.56 is the average of table 6 where the interval width was also taken into account.

Centrality (%)	N_{ch}/η	N_{part}
0 - 5	44.6	18.5
5 - 10	35.9	15.8
10 - 20	30.0	13.65
20 - 40	23.0	10.5
40 - 60	15.8	7.0
60 - 80	9.7	4.0
80 - 100	4.2	2.3

Table 6: Glauber parameters for $\sqrt{s} = 5$ TeV [41].

Then a fluctuation of multiplicity was determined by assuming the deviation to be $\sigma = (N_{ch_i})^{0.7}$. The final N_{ch} was then sampled from a Gaussian with the previously determined σ and $\mu = N_{ch_i}$. The number of J/Ψ particles was set equal to N_{ch} . The number of binary collisions was determined by creating again a `TGraph` using the centralities and N_{part} from table 6. This

time a fit was made through the points. This function then was evaluated at the given centrality so that one obtained N_{part} and therefore $N_{bin} = N_{part} - 1$.

In the next step the `TLorentzVector` for lead was set to $(0, 0, -p_{Pb}, sc \cdot E_{Pb})$ where a scale factor $sc = (N_{bin})^{0.7}$ was taken into account. The energy was $E_{Pb} = 1580$ GeV and the momentum was calculated as

$$p_{Pb} = \sqrt{(sc \cdot E_{Pb})^2 + (sc \cdot m_p)^2} \quad (38)$$

Using the two Lorentz vectors, the center-of-mass boost vector can be created just as before. The generation of the direction of the charged particles also was done just as in section 3.2. The Bjorken boost was executed differently, the three parameters were just optimized in order to make the result look as good as possible. The charged particles got boosted with the center-of-mass and Bjorken boost. Hereby the Gauss z rapidity was not taken into account, only the Bjorken z rapidity with $R_B^y = 2.8$ was used in order to boost. Finally the same plots as in section 3.4 were made.

In the end, every step was repeated but with opposite direction of the proton and lead momenta.

4.4.1 Results

In figure 31 and 32 the results of this simulation are presented.

For the J/Ψ yield, the general shape of the distribution is just like in the publication. The crossing of the two branches seems to happen at the same multiplicity as in the ALICE data. The two distributions of the simulation though are not as close to each other as the two published distributions. Nevertheless, the result of the massive target model is very well fitting the data.

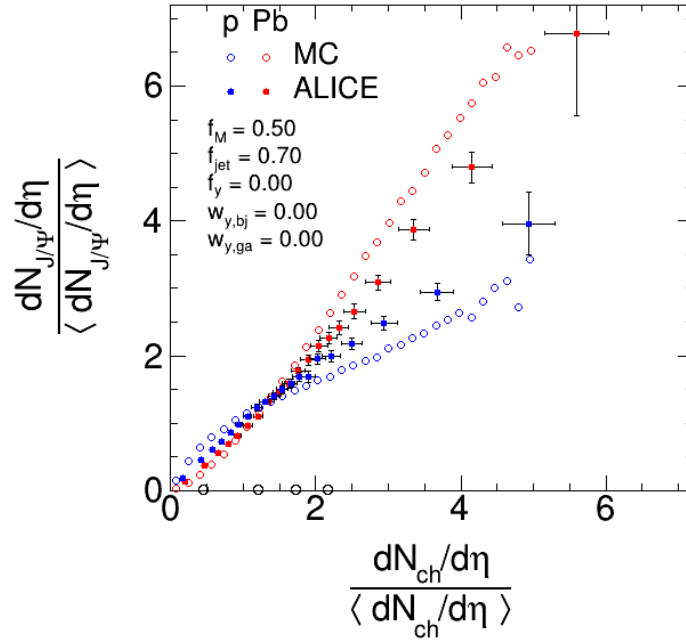


Figure 31: J/Ψ yield as a function of the normalized charged particle pseudorapidity density. Filled dots indicate ALICE measurement presented in section 1.4. Open markers represent results from the massive target MC simulation. In both cases, blue represents the p-going direction while red stands for the Pb-going direction.

In the distribution of the mean transverse momentum $\langle p_T \rangle$ at $dN_{ch}/d\eta \approx 1.1$ and higher, the $\langle p_T \rangle$ measured in proton going direction is greater than in the lead going direction just as measured at ALICE. The gap of the values measured in the two opposite directions is mostly smaller than

given in the data. At $dN_{ch}/d\eta > 4.0$ there is not a clear pattern that both $\langle p_T \rangle$ distributions from the simulation seem to follow, there is no saturation reached. In contrast to the measured data, the mean transverse momentum measured in the lead going direction at low $dN_{ch}/d\eta$ is higher than when measured in proton going direction. In the latter, the upwards going tendency at low charged particle multiplicity shows just as in the data.

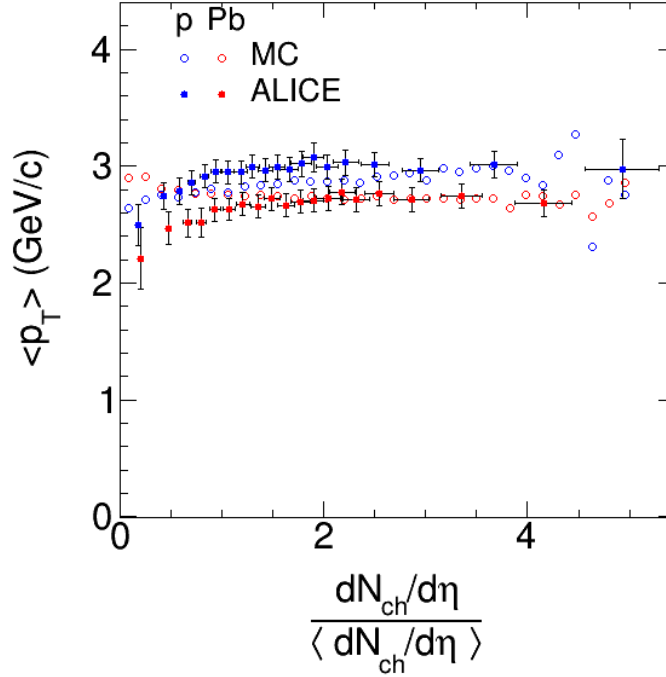


Figure 32: Mean transverse momentum $\langle p_T \rangle$ versus the normalized charged particle pseudorapidity density. Filled dots indicate ALICE measurement presented in section 1.4. Open markers represent results from the massive target MC simulation. In both cases, blue represents the p-going direction while red stands for the Pb-going direction.

4.5 Comparison

The two models made a different approach in order to explain the behaviour seen in section 1.4. The general process in both codes is the same, meaning generating the directions of the particles and setting the Lorentz vectors, creating a charged particle loop with a Bjorken and center-of-mass boost and filling the histograms. The main difference is that in the model described in section 4.4, the collision consists of the proton and a massive target while in the model described in section 3, the collision consists of the proton colliding successively with single lead nucleons. This difference is reflected in the code by sampling the number of participants from the distribution created using a Glauber Monte Carlo approach in section 2. From that the number of binary collisions was determined. Then in each binary collision, the protons energy varied and was described using the function 37. The number of charged particles was also dependent on the new energy \sqrt{s} . On the other hand in the code describing the massive target model, N_{coll} was determined by sampling the centrality. From this quantity, the number of charged particles could also be determined. The protons energy was fixed, therefore the Lorentz vector of the proton was fixed. The Bjorken boost parameters were constant too. The Lorentz vectors of the lead nucleons though differed: A scale factor was introduced which took the number of binary collisions into account and which was then

multiplied by the energy and mass. For this reason the center-of-mass boost was not constant for every event. The lead Lorentz vector on the other hand was constant for the multiple collision model but the center-of-mass boost was not due to the protons energy decrease.

Both models qualitatively describe the data well: In the results of both models there is the clear splitting which appears in the actual ALICE data in the J/Ψ yield as well as in the $\langle p_T \rangle$ distribution. The magnitudes of the $\langle p_T \rangle$ values and the yield also match the data. Nevertheless the results of the two models look quite differently. For the J/Ψ yield at low multiplicities, in the massive target model the crossing happens at the same multiplicity as in the data while in the multiple collision model, the distributions cross at much higher multiplicities. In contrast, the distribution of the transverse momentum p_T from the multiple collision model at multiplicities greater than 1 fits the data much better than the second model. The detailed shape of the particle source and the way the boosting is modeled is important for a more precise description of the data.

5 Conclusion and Outlook

Studying proton lead collisions at ALICE has shown that there is a difference in the J/Ψ yield and the transverse momentum as a function of the normalized charged particle multiplicity density depending on the direction that is measured in (section 1.4). The goal of this bachelors thesis was to reconstruct this behaviour using a Monte Carlo simulation. Understanding the properties of the J/Ψ meson is an important aspect for gaining knowledge about the QGP created in laboratories. In the first part of this thesis a Glauber Monte Carlo simulation was written. Herein the position of 208 lead nucleons was set randomly by sampling the radius from the Woods-Saxon density distribution and the azimuthal and polar angles. The proton was set at position (0,0,0). The nucleus and proton were then shifted by half of the impact parameter which was sampled too. Then the transverse distance between the protons position and all the lead nucleons was calculated in order to say whether a collision takes place. For this purpose two different collision profiles were regarded. The first one is the hard sphere profile where a collision always takes place when the transverse distance is below a certain distance. The second profile is the realistic or Gauss profile where the probability of a collision is not either 0 or 1 but given by a Gaussian function. Using these methods the number of participants was determined resulting in a N_{part} probability distribution.

This distribution was then used to sample the number of participants and therefore to also determine the number of collisions. The main aspect in this simulation was that the proton lead collision is regarded as multiple consecutive binary nucleon-nucleon collisions in which the proton energy decreases with every collision. Therefore a loop was created to step through each of the collisions. In this loop the protons energy was described by a function whose parameters were obtained by fitting the pseudorapidity distributions at different centralities to the corresponding distributions measured at ALICE. Accordingly the total center-of-mass energy \sqrt{s} was decreasing with every binary collision, reaching a minimum of 0.1 TeV.

At each binary collision, the number of charged particles was determined. For this in the beginning two probability distributions measured at ALICE at $\sqrt{s} = 7$ TeV and $\sqrt{s} = 0.9$ TeV were given. They were used in order to make a linear extrapolation which led to a two dimensional histogram shown in figure 18b. From this histogram, one can obtain the charged particle multiplicity probability distribution at energies between 0 TeV and 7 TeV. The direction of propagation and the transverse momentum of each charged particle were then sampled. For the latter, two Levy functions with different temperatures were used to model the soft and hard components. Afterwards the charged particles were boosted with a center-of-mass boost vector and a so called Bjorken boost. There were three parameters for this boost which were determined by fitting η distributions to p-p data at four different energies. The rapidity y_z which determined the boost vector was then multiplied by 0.25 in order to make the $p_T - \eta$ distributions less wide. The overall width of the eta distribution turned out to be essential to reproduce the trends of the two measured distributions. The center-of-mass boost vector was created by adding the four vector of the proton and the lead nucleus. Due to the decreasing proton energy, the center-of-mass shifted from the proton to the lead nucleus.

In the end the properties of the charged particles were represented in histograms considering the detectors acceptance.

Lastly another approach was looked at. Here, the energy of the proton was not changing but fixed at 4000 GeV. The collision was looked at as a collision with a massive target. The number of charged particles was evaluated from the centrality which was generated randomly. The charged particles were then also boosted twice but with different parameters. In the end, the same properties as before were shown in histograms.

The results of the first model are presented in section 4. The splitting in both the $\langle p_T \rangle$ distribution and the J/Ψ yield were visible. The magnitude of the splitting in the $\langle p_T \rangle$ distribution also matches the data. The shape in the $\langle p_T \rangle$ distribution was at low multiplicities different to the at ALICE measured distributions: The $\langle p_T \rangle$ measured in lead going direction was decreasing instead of increasing. In the J/Ψ yield, the overall shape also fitted the data. The crossing of the two in opposite direction going distributions took place at a higher multiplicity than indicated by the ALICE measurement. In general one can say that this relatively simple model can reproduce the overall shape of the published distributions and achieves even quantitatively good results. The main aspects which led to the splitting behaviour were the boosting and the decreasing proton energy which results in a center-of-mass shift. The detectors acceptance also plays an important role as demonstrated in section 3.2 and 30.

In the second model with the massive target, the results are shown in section 4.4.1. Here the splitting could also be seen. The general shape of the J/Ψ yield was as the shape of the actual data. The p_T distribution showed a slightly different behaviour at lower multiplicities but from there on, the splitting between the two directions was visible.

There are further steps to improve this simulation which can be considered. One of them would be to try out different energy loss functions which could possibly describe the data better. In addition, a third boost could be considered in order to take the nucleon momentum into account. This could be sampled from the effective spectral function of ^{208}Pb . A minimizer could also be used to optimize the parameters by minimizing the χ^2 of the $\langle p_T \rangle$ and the J/Ψ yield distributions, for example the parameters of the energy function or the parameters of the Bjorken boost. Since the width of the η distribution is essential, more detailed studies regarding this are necessary in the future.

6 Appendix

6.1 Kinematics

Derivation of equation 20 using definitions of hyperbolic functions [42]:

$$\begin{aligned} \sinh(x) &= \frac{1}{2} (e^x - e^{-x}) \\ \cosh(x) &= \frac{1}{2} (e^x + e^{-x}) \end{aligned} \quad (39)$$

Then using equation 17 one can write:

$$\begin{aligned} e^y &= e^{\frac{1}{2} \ln\left(\frac{E+p_L}{E-p_L}\right)} = \left(e^{\ln\left(\frac{E+p_L}{E-p_L}\right)} \right)^{\frac{1}{2}} = \sqrt{\frac{E+p_L}{E-p_L}} \\ e^{-y} &= \left(e^{-\ln\left(\frac{E+p_L}{E-p_L}\right)} \right)^{\frac{1}{2}} = \left(e^{\ln\left(\frac{E-p_L}{E+p_L}\right)} \right)^{\frac{1}{2}} = \sqrt{\frac{E-p_L}{E+p_L}} \end{aligned} \quad (40)$$

Looking at figure 25, the hypotenuse p is:

$$p = \sqrt{p_T^2 + p_L^2} \quad (41)$$

The transverse mass can be written using the third binomial formula as

$$m_T = \sqrt{m^2 + p_T^2} = \sqrt{m^2 + p^2 - p_L^2} = \sqrt{E^2 - p_L^2} = \sqrt{(E-p_L)(E+p_L)} \quad (42)$$

Combining these leads to the relations shown in equation 20:

$$\begin{aligned} m_T \cdot \cosh(y) &= \frac{m_T}{2} \left(\sqrt{\frac{E+p_L}{E-p_L}} + \sqrt{\frac{E-p_L}{E+p_L}} \right) \\ &= \frac{\sqrt{(E-p_L)(E+p_L)}}{2} \left(\sqrt{\frac{E+p_L}{E-p_L}} + \sqrt{\frac{E-p_L}{E+p_L}} \right) \\ &= \frac{1}{2} \left(\sqrt{\frac{(E+p_L)(E-p_L)(E+p_L)}{E-p_L}} + \sqrt{\frac{(E-p_L)(E-p_L)(E+p_L)}{E+p_L}} \right) \\ &= \frac{1}{2} (E+p_L + E-p_L) \\ &= E \end{aligned} \quad (43)$$

$$\begin{aligned} m_T \cdot \sinh(y) &= \frac{m_T}{2} \left(\sqrt{\frac{E+p_L}{E-p_L}} - \sqrt{\frac{E-p_L}{E+p_L}} \right) \\ &= \frac{\sqrt{(E-p_L)(E+p_L)}}{2} \left(\sqrt{\frac{E+p_L}{E-p_L}} - \sqrt{\frac{E-p_L}{E+p_L}} \right) \\ &= \frac{1}{2} \left(\sqrt{\frac{(E+p_L)(E-p_L)(E+p_L)}{E-p_L}} - \sqrt{\frac{(E-p_L)(E-p_L)(E+p_L)}{E+p_L}} \right) \\ &= \frac{1}{2} (E+p_L - E+p_L) \\ &= p_L \end{aligned} \quad (44)$$

For the relations containing η , figure 25 has to be taken into account again to see:

$$\begin{aligned} \tan \theta &= \frac{p_T}{p_L} \\ \rightarrow p_L &= \frac{p_T}{\tan \theta} \end{aligned} \quad (45)$$

From equation 19 follows:

$$\begin{aligned} \theta &= 2 \tan^{-1} (e^{-\eta}) \\ p_L &= \frac{p_T}{\tan (2 \tan^{-1} (e^{-\eta}))} \end{aligned} \quad (46)$$

Then one can use the following trigonometric identity [42]:

$$\tan(2\alpha) = \frac{2 \tan \alpha}{1 - \tan^2 \alpha} \quad (47)$$

so that p_L results as

$$\begin{aligned} p_L &= \frac{p_T}{\frac{2 \tan (\tan^{-1}(e^{-\eta}))}{1 - \tan^2(\tan^{-1}(e^{-\eta}))}} \\ &= \frac{p_T}{\frac{2 e^{-\eta}}{1 - (e^{-\eta})^2}} \\ &= \frac{p_T}{2} \frac{1 - (e^{-\eta})^2}{e^{-\eta}} \\ &= \frac{p_T}{2} e^{\eta} (1 - (e^{-\eta})^2) \\ &= p_T \frac{1}{2} (e^{\eta} - e^{-\eta}) \\ &= p_T \sinh \eta \end{aligned} \quad (48)$$

Using this and the relation [42]

$$\sinh^2(x) + \cosh^2(x) = 1 \quad (49)$$

the following relation can be derived:

$$\begin{aligned} p &= \sqrt{p_T^2 + p_L^2} \\ &= \sqrt{p_T^2 + p_T^2 \sinh^2 \eta} \\ &= p_T \sqrt{1 + \sinh^2 \eta} \\ &= p_T \cosh \eta \end{aligned} \quad (50)$$

References

- [1] Wolfgang Demtröder. *Experimentalphysik 4 - Kern-, Teilchen- und Astrophysik*. 5th ed. 2016.
- [2] Mark Thomson. *Modern Particle Physics*. 4th ed. 2019.
- [3] Jana Crkovska. *Study of the J/Ψ production in pp collisions at $\sqrt{s} = 5.02$ TeV and of the J/Ψ production multiplicity dependence in p-Pb collisions at $\sqrt{s_{NN}} = 8.16$ TeV with ALICE at the LHC*. http://cds.cern.ch/record/2651031/files/CERN-THESIS-2018-281_2.pdf?version=1. 2018.
- [4] CERN. <https://home.cern/science/physics/standard-model>. last looked at 19.02.2022.
- [5] CERN. <https://home.cern/science/physics/dark-matter>. last looked at 27.01.2022.
- [6] J. E. Augustin et al. “Discovery of a Narrow Resonance in e^+e^- Annihilation”. In: *Phys. Rev. Lett.* 33 (1974), pp. 1406–1408. DOI: 10.1103/PhysRevLett.33.1406.
- [7] J. J. Aubert et al. “Experimental Observation of a Heavy Particle J ”. In: *Phys. Rev. Lett.* 33 (1974), pp. 1404–1406. DOI: 10.1103/PhysRevLett.33.1404.
- [8] The Royal Swedish Academy of Sciences. <https://www.nobelprize.org/prizes/physics/1976/press-release/>. 1976.
- [9] Particle Data Group. *$c\bar{c}$ Mesons*. <https://pdg.lbl.gov/2017/tables/rpp2017-tab-mesons-c-cbar.pdf>. 2017.
- [10] T. Matsui and H. Satz. “ J/ψ Suppression by Quark-Gluon Plasma Formation”. In: *Phys. Lett. B* 178 (1986), pp. 416–422. DOI: 10.1016/0370-2693(86)91404-8.
- [11] Anton Andronic et al. “The multiple-charm hierarchy in the statistical hadronization model”. In: *JHEP* 07 (2021), p. 035. DOI: 10.1007/JHEP07(2021)035. arXiv: 2104.12754 [hep-ph].
- [12] J. Stachel. *Quarkonium production at the phase boundary – a signal of deconfinement*. <http://ift.uni.wroc.pl/~cpod2016/Stachel.pdf>. 2016.
- [13] A. Andronic et al. “Evidence for charmonium generation at the phase boundary in ultra-relativistic nuclear collisions”. In: *Phys. Lett. B* 652 (2007), pp. 259–261. DOI: 10.1016/j.physletb.2007.07.036. arXiv: nucl-th/0701079.
- [14] A. Andronic. “Decoding the phase structure of QCD via particle production at high energy”. In: *Nature* 561 (2018), pp. 321–330. DOI: 10.1038/s41586-018-0491-6.
- [15] ATLAS. <https://atlas.cern/glossary/mass>. last looked at 22.02.2022.
- [16] Shreyasi Acharya et al. “ J/ψ production as a function of charged-particle multiplicity in p-Pb collisions at $\sqrt{s_{NN}} = 8.16$ TeV”. In: *JHEP* 09 (2020), p. 162. DOI: 10.1007/JHEP09(2020)162. arXiv: 2004.12673 [nucl-ex].
- [17] ALICE. <https://alice.cern/#experiment>. last looked at 19.02.2022.
- [18] ALICE. <https://alice.cern/node/5531>. last looked at 28.01.2022.
- [19] ALICE. <https://alice.cern/node/5534>. last looked at 28.01.2022.
- [20] ALICE. <https://alice.cern/node/5500>. last looked at 28.01.2022.
- [21] ALICE. <https://cds.cern.ch/record/2628419/plots>. last looked at 28.01.2022.
- [22] ALICE. <https://alice.cern/node/5494>. last looked at 28.01.2022.
- [23] ALICE. <https://alice.cern/node/5535>. last looked at 28.01.2022.
- [24] ALICE. <https://alice.cern/node/5515>. last looked at 31.01.2022.

- [25] IBM. <https://www.ibm.com/cloud/learn/monte-carlo-simulation>. last looked at 01.02.2022.
- [26] Chad Rexrode. *Monte-Carlo Glauber Model Simulations of Nuclear Collisions*. <https://digitalcommons.calpoly.edu/cgi/viewcontent.cgi?referer=&httpsredir=1&article=1113&context=physsp>. 2014.
- [27] Yasser Corrales Morale. *Identified hadron production in pp collisions measured with ALICE*. <https://root.cern>. 2017.
- [28] Q. Y. Shou et al. “Parameterization of Deformed Nuclei for Glauber Modeling in Relativistic Heavy Ion Collisions”. In: *Phys. Lett. B* 749 (2015), pp. 215–220. DOI: 10.1016/j.physletb.2015.07.078. arXiv: 1409.8375 [nucl-th].
- [29] Maciej Rybczynski and Wojciech Broniowski. “Wounded nucleon model with realistic nucleon-nucleon collision profile and observables in relativistic heavy-ion collisions”. In: *Phys. Rev. C* 84 (2011), p. 064913. DOI: 10.1103/PhysRevC.84.064913. arXiv: 1110.2609 [nucl-th].
- [30] Jaroslav Adam et al. “Centrality dependence of particle production in p-Pb collisions at $\sqrt{s_{NN}} = 5.02$ TeV”. In: *Phys. Rev. C* 91.6 (2015), p. 064905. DOI: 10.1103/PhysRevC.91.064905. arXiv: 1412.6828 [nucl-ex].
- [31] Adam Bzdak and Vladimir Skokov. “Decisive test of color coherence in proton-nucleus collisions at the LHC”. In: *Phys. Rev. Lett.* 111 (2013), p. 182301. DOI: 10.1103/PhysRevLett.111.182301. arXiv: 1307.6168 [hep-ph].
- [32] Sangyong Jeon and Joseph Kapusta. “Linear extrapolation of ultrarelativistic nucleon-nucleon scattering to nucleus-nucleus collisions”. In: *Physical Review C* 56.1 (July 1997), pp. 468–480. ISSN: 1089-490X. DOI: 10.1103/physrevc.56.468. URL: <http://dx.doi.org/10.1103/PhysRevC.56.468>.
- [33] Klaus Reygers. “Teilchenproduktion in ultrarelativistischen p+Pb- und Pb+Pb- Reaktionen”. PhD thesis. Westfälische Wilhelms-Universität Münster, 1999.
- [34] “Charged-particle multiplicity measurement with Reconstructed Tracks in pp Collisions at $\sqrt{s} = 0.9$ and 7 TeV with ALICE at the LHC”. In: (July 2013).
- [35] Sumit Basu et al. “Multiplicity and pseudorapidity density distributions of charged particles produced in pp, pA and AA collisions at RHIC & LHC energies”. In: *J. Phys. G* 48.2 (2020), p. 025103. DOI: 10.1088/1361-6471/abc05c. arXiv: 2008.07802 [nucl-ex].
- [36] Dennis Weiser. *Inclusive J/Ψ production at mid-rapidity in pp and Pb–Pb collisions with ALICE*. https://www.physi.uni-heidelberg.de/Publications/Dissertation_Dennis_Weiser.pdf. 2019.
- [37] J. D. Bjorken. “Highly relativistic nucleus-nucleus collisions: The central rapidity region”. In: *Phys. Rev. D* 27 (1 Jan. 1983), pp. 140–151. DOI: 10.1103/PhysRevD.27.140. URL: <https://link.aps.org/doi/10.1103/PhysRevD.27.140>.
- [38] H. Basler. *Relativistic hydrodynamics and the Bjorken model*. <http://crunch.i kp.physik.tu-darmstadt.de/nhc/pages/lectures/rhiseminar09-10/basler.pdf>. 2010.
- [39] Yasser Corrales Morales. “Identified hadron production in pp collisions measured with ALICE”. In: *J. Phys. Conf. Ser.* 878.1 (2017), p. 012005. DOI: 10.1088/1742-6596/878/1/012005.
- [40] Shreyasi Acharya et al. “Charged-particle production as a function of multiplicity and transverse sphericity in pp collisions at $\sqrt{s} = 5.02$ and 13 TeV”. In: *Eur. Phys. J. C* 79.10 (2019), p. 857. DOI: 10.1140/epjc/s10052-019-7350-y. arXiv: 1905.07208 [nucl-ex].

- [41] Thomas A. Trainor. “Glauber-model analysis of 5 TeV **p**-Pb centrality compared to a two-component (soft + hard) model of hadron production in high-energy nuclear collisions”. In: (Jan. 2018). arXiv: 1801.05862 [hep-ph].
- [42] Eberhard Zeidler. *Springer-Taschenbuch der Mathematik*. Wiesbaden: Springer Vieweg, 2013. DOI: <https://doi.org/10.1007/978-3-8348-2359-5>.

Acknowledgement

I would like to thank the ALICE group for giving me the opportunity of writing my bachelors thesis.

I also want to thank Prof. Dr. Klaus Reygers for the help I got and the interesting discussions.

Thank you to Priv. Doz. Dr. Yvonne Pachmayer for being the second referee for my thesis.

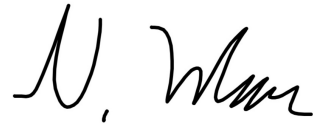
I am also very thankful for the help of my supervisor Dr. Alexander Schmah. You really motivated me and without you, this thesis wouldn't be possible.

Lastly I want to thank my family for supporting me during my studies.

Erklärung

Ich versichere, dass ich diese Arbeit selbstständig verfasst und keine anderen als die angegebenen Quellen und Hilfsmittel benutzt habe.

Heidelberg, den 04. März 2022,

A handwritten signature in black ink, appearing to read 'U. Müller'.